Department of Chemistry — Radiochemistry
University of Helsinki
Finland

Metal(IV) Phosphate Based Functional Materials for Selectively Harvesting Rare-Earth Elements from Bauxite Residue

Wenzhong Zhang

ACADEMIC DISSERTATION

To be presented, with the permission of the Faculty of Science of the University of Helsinki, for public examination in lecture hall A129 at Chemicum, A. I. Virtasen Aukio 1, on 23rd November 2018, at 12 noon.

Helsinki 2018

Supervisors **University Researcher, Docent Risto T. Koivula, Ph.D.**
Senior Lecturer, Professor (H.C.) Risto O. Harjula, Ph.D.
Ion-Exchange for Nuclear Waste Treatment and for Recycling
Department of Chemistry — Radiochemistry
Faculty of Science
University of Helsinki, Finland

Pre-examiners **Assistant Professor Mari Lundström, D.Sc. (Tech.)**
Hydrometallurgy and Corrosion
Department of Chemical and Metallurgical Engineering
Aalto University, Finland

Professor Giuseppe Modolo, Ph.D.
Nuclear Waste Management and Reactor Safety
Institute of Energy and Climate Research
Forschungszentrum Jülich GmbH, Germany

Dissertation Opponent **Professor Freddy Kleitz, Dr. rer. nat.**
Department of Inorganic Chemistry — Functional Materials
Faculty of Chemistry
University of Vienna, Austria

ISSN 0358-7746
ISBN 978-951-51-4650-2 (paperback)
ISBN 978-951-51-4651-9 (PDF)
http://ethesis.helsinki.fi/

Unigrafia
Helsinki 2018

There is a tide in the affairs of men,
Which taken at the flood, leads on to fortune.
Omitted, all the voyage of their life is bound in shallows and in miseries.
On such a full sea are we now afloat.
And we must take the current when it serves, or lose our ventures.

William Shakespeare

Abstract

Inorganic metal(IV) phosphates with adjustable structural features, strong acid resistance and selective ion-exchange capabilities are an ideal class of materials to be applied in solid-liquid metal separation processes. The surface hydroxyl groups with ion-exchange capability also grant the metal(IV) phosphates with vast possibilities for further functionalisation and hybridisation.

Rare-earth elements (REEs), made up by scandium (Sc), yttrium and the entire lanthanide series, are irreplaceable enablers for the transition to a low-carbon economy. Pure fractions of REEs are, until today, vital components in high-tech applications such as electric motors. The ever-growing demands for REEs are restricted by limited mining productions and regulated cross-border trading.

Bauxite residue (BR), the waste generated from the industrial production of alumina, are stockpiled in enormous quantity across the globe. Certain types of BR are considered as exploitable REE reservoirs since they contain minable concentrations of REEs. To harvest the REEs contents from BR, the metals are typically leached by mineral acids before further separations. However, the recovery of REEs from the acidic leachates is challenging due to low concentrations of REEs and high concentrations of other interfering metals.

The dissertation summarised the design and application of various functional materials based on metal(IV) phosphate for separation processes relating to the recovery of REEs from BR leachates. Traditional inorganic titanium and zirconium phosphate materials with amorphous and layered crystalline structures were firstly tested for selective Sc separation. Although these materials preferentially exchange Sc^{3+} compared to all other investigated metal ions, the internal interlayer surfaces were unavailable to Sc^{3+} in the case of the crystalline materials. To fully utilise their ion-exchange sites, titanium phosphate moieties were functionalised onto the surfaces of mesoporous MCM-41 silica. Inspired by the structure of solvating extractant tri-*n*-butylphosphate (TBP), short *n*-alkyl chains were grafted onto the titanium phosphate grafts to mimic TBP structure. Batch tests confirmed the solvating extraction capability of the obtained solid material, with excellent

performance for separating Sc^{3+} and lanthanide ions. Hybrid titanium di-*n*-butylphosphate coordination polymers were prepared and they exhibited exceptional intralanthanide separation capability. The selective uptake of smaller lanthanide ions was resulted from a transmetalation process, where the lanthanide ions substituted the framework titanium-oxo clusters. An almost quantitative separation between neodymium and dysprosium was demonstrated by simply controlling the solution pH in a batch system.

A multitude of characterisation methods were utilised to study and confirm the compositional and structural properties of the newly synthesised materials and their metal separation mechanisms. Functional materials assembled on the metal(IV) phosphate platform offer versatile functionalities and alterable metal uptake mechanisms that are suitable for hydrometallurgical separation of the REEs.

Acknowledgements

The work summarised in this dissertation has been carried out in the iX group, Department of Chemistry—Radiochemistry at University of Helsinki. The research leading to these results has received funding from the European Community's Horizon 2020 Programme under Grant Agreement no. 636876 (Marie Skłodowska-Curie Actions-European Training Network for Zero-Waste Valorisation of Bauxite Residue). Additional supports from the Doctoral Programme in Chemistry of Molecular Sciences (dissertation completion and travel grants) and from the COST Action CM1206 (short-term scientific mission grant) are gratefully acknowledged.

I owe a great debt of gratitude to my supervisor, the late *Professor Risto Harjula*. It was you who introduced me to the fascinating world of ion-exchange materials. Knocking on your office door always turned my depressed feelings into joyful recognition. Forever will I remember your motto that chemistry is not about publishing papers, but to make the world a better place. My work would not have been possible without my supervisor *Dr. Risto "Ripa" Koivula*, who took over the leadership of our group in 2017. *Ripa*, you continuously supported my wildest ideas and are always there to help. It has been an absolute great pleasure to work under your guidance. Thanks for supporting me while generously allowing sufficient degree of freedom.

The persons and dynamics in our iX group are always inspiring. Especially, I thank *Junhua* and *Elmo* who share my common interests of metal phosphates and badminton. I cannot image going through the PhD process without you guys. I appreciate the company of my officemate *Satu*, who have an absolute patience to my complaints about experiments. Among others, I thank also *Valtteri*, *Ilkka, Leena (M.), Anna-Elina* and *Sanna* for insightful and cheerful discussions, both academically and personally.

Within the radiochemistry unit, everyone has been helpful and kind. Many thanks to *Professor Jukka Lehto* and *Senior Lecturer Marja "Maikki" Siitari-Kauppi* for offering invaluable support, guidance and advices. I sincerely thank *Professor Gareth Law* for being the Custos and *Associate Professor Anu Airaksinen* for taking care of the dissertation-related procedures.

I am greatly thankful to *Professor Freddy Kleitz* who kindly agreed to be the opponent of my public examination. Sincere thanks are in place for the two pre-examiners, *Assistant*

Professor Mari Lundström and *Professor Giuseppe Modolo* who have given insightful comments and suggestions to finalise the dissertation.

I would like to acknowledge my wonderful colleagues and collaborators. Locally speaking, I thank *Timo Hatanpää*, *Dr. Sami Hietala*, *Dr. Juhani Virkanen* and the late *Dr. Leonid Khriachtchev* for sharing their expertise. Within the REDMUD family, my research visits would not have been possible without *Dr. Dženita Avdibegović* (proudly made it before me!), *Dr. Mercedes Regadío* and *Professor Koen Binnemans* (KU Leuven), *Bengi Yagmurlu* and *Carsten Dittrich* (MEAB), and *Chiara Bonomi* and *Professor Dimitrios Panias* (National Technical University of Athens). These secondments not only were eye-opening in scientific aspects, but also exposed me to different culture in the Europe. I wish to extend my sincere appreciation to everyone involved in the REDMUD project.

Over the years of my PhD study, the shared joy from our Chinese community on the Kumpula hill has been an irreplaceable part of my life. For that, I thank (in the order of appearance) *Zhongmei*, *Hangzhen*, *Chao*, *Xiaodong*, *Ming*, *Jingwen*, among others. In addition, the time spent with *Junjie*, *Yan*, *Xiaoxu* and *Xun* was always filled with genuine laughter (and more often wholeheartedly sarcasms).

My journey in research all started thanks to my supervisor in bachelor and master studies, *Professor Fang Xu*. Your attitudes towards science and life continue to inspire me till this very moment and beyond.

I cherish the unwavering support of my family, more specifically my parents and my grandparents. Being the youngest of my generation (11/11) in our family is a privilege that I continue to enjoy, and I do wish to convey my gratitude to everyone.

“With every step you climb another mountain, every breath it is harder to believe. You make it through the pain, weather the hurricanes, to get to that one thing.” There are no boundaries in science, and Ph.D. is merely the beginning.

Warsaw, August 12th, 2018



Wenzhong Zhang

List of Original Publications

This dissertation is based on the following articles:

I. W. Zhang, R. Koivula, E. Wiikinkoski, J. Xu, S. Hietala, J. Lehto, R. Harjula, **Efficient and Selective Recovery of Trace Scandium by Inorganic Titanium Phosphate Ion-Exchangers from Leachates of Waste Bauxite Residue.** *ACS Sustainable Chemistry & Engineering* **2017**, 5 (4), 3103—3114.

II. D. Avdibegović[#], W. Zhang[#], J. Xu, M. Regadío, R. Koivula, K. Binnemans, **Selective Ion-Exchange Separation of Sc(III) over Fe(III) by Crystalline α-Zirconium Phosphate Platelets Under Acidic Conditions.** *Manuscript.*

III. W. Zhang[#], D. Avdibegović[#], R. Koivula, T. Hatanpää, S. Hietala, M. Regadío, K. Binnemans, R. Harjula, **Titanium Alkylphosphate Fuctionalised Mesoporous Silica for Enhanced Uptake of Rare-Earth Ions.** *Journal of Materials Chemistry A* **2017**, 5, 23805—23814.

IV. W. Zhang, S. Hietala, L. Khriachtchev, T. Hatanpää, B. Doshi, R. Koivula, **Intralanthanide Separation on Layered Titanium(IV) Organophosphate Materials *via* a Selective Transmetalation Process.** *ACS Applied Materials & Interfaces* **2018**, 10, 22083—22093.

# Equal contribution

The articles are referred to in the text by their roman numerals.

Author contributions:

I. R.H., R.K. and W.Z. conceived the research. W.Z., E.W. and J.X. synthesised the materials. W.Z. conducted all other experiments, except that S.H. performed the NMR analysis. W.Z., R.K. and R.H. interpreted the data. W.Z. wrote the manuscript. R.K., S.H., J.L. and R.H. commented on the manuscript.

II. D.A., W.Z., R.K. and K.B. conceived the research. D.A., W.Z. and J.X. performed all experiments. D.A. and W.Z. analysed the data and D.A. drafted the manuscript. All authors commented on the manuscript.

III. W.Z., D.A., K.B and R.K. conceived the research. W.Z. and D.A. perfomed all experiments, except that T.H. conducted thermogravimetry analysis and S.H. conducted NMR analysis. W.Z. and D.A. analysed the data and W.Z. drafted the manuscript. All authors commented on the manuscript.

IV. W.Z. and R.K. conceived the research. W.Z. performed all experiments, except that S.H. performed NMR spectroscopy, L.K. supervised Raman microscopy, T.H. conducted thermogravimetry analysis and B.D. performed BET experiments. W.Z. analysed the data and drafted the manuscript with the inputs and comments from all other authors.

Abbreviations

am-TiP	amorphous titanium phosphate
BET	Brunauer, Emmett and Teller
BR	bauxite residue
CRM	critical raw material
DBP	di-*n*-butyl phosphate (deprotonated)
EA	elemental analysis (or analyser)
EDX	energy-dispersive X-ray spectroscopy
EU	European Union
EXAFS	extended X-ray absorption fine structure
FE-SEM	field emission-scanning electron microscope (or microscopy)
FTIR	Fourier transform infrared spectroscopy
HDBP	di-*n*-butyl phosphate (protonated)
ICP-MS	inductively coupled plasma-mass spectrometry
ICP-OES	inductively coupled plasma-optical emission spectroscopy
IUPAC	International Union of Pure and Applied Chemistry
M41	MCM-41 silica
MAS	magic angel spinning
MP-AES	microwave plasma-atomic emission spectrometer (or spectrometry)
NMR	nuclear magnetic resonance
NORM	naturally occurring radioactive material
PLS	pregnant leaching solution
REE	rare-earth element
SX	solvent extraction
TBP	tri-*n*-butyl phosphate
TG	thermogravimetry
TiP	titanium phosphate
XRD	X-ray diffraction
ZrP	zirconium phosphate

Note: the list does not include either parameters or standard chemical formulae.

Table of Contents

Abstract i
Acknowledgements iii
List of Original Publications v
Abbreviations vii
Table of Contents viii
1 Introduction 1
1.1 A Recap of the Rare-Earth Elements 1
1.1.1 Natural Occurrence and Deposits 4
1.1.2 Applications and Criticality 5
1.1.3 Technosphere Mining 7
1.2 Bauxite Residue: A Waste or Resource? 7
1.2.1 Disposal, Storage and Remediation 9
1.2.2 Rare Earth Contents in Bauxite Residue 10
1.2.3 Near-Zero-Waste Valorisation of Bauxite Residue 11
1.3 Hydrometallurgical Separation and Recovery of Rare-Earth Elements 11
1.3.1 Acid Leaching 12
1.3.2 Selective Precipitation 13
1.3.3 Solvent Extraction 13
1.3.4 Ion-Exchange 15
1.3.5 Recovery methods 16
1.4 Metal(IV) Phosphate Materials 16
1.4.1 Titanium Phosphate Materials 17
1.4.2 Ion-Exchange and Intercalation 18
1.4.3 Design and Functionalisation of the Materials 19
2 Aim of the Study 21
3 Experimental 22
3.1 Experimental Design 22
3.2 Materials Synthesis 24

3.2.1 Inorganic Metal(IV) Phosphates 24
3.2.2 MCM-41 Silica Grafted Titanium Alkylphosphates 25
3.2.3 Hybrid Titanium Butylphosphates 26
3.3 Supporting Characterisations 26
3.3.1 Morphological and Compositional Characterisations 26
3.3.2 Structural Characterisations 27
3.4 Separation Studies 28
3.4.1 Batch Experiments 28
3.4.2 Column Experiments 30
4 Results and Discussion 31
4.1 Materials Characterisations 31
4.1.1 Morphologies and Compositions 32
4.1.2 Structure 34
4.1.3 Summary 38
4.2 Batch Experiments 39
4.2.1 Titanium Phosphates 39
4.2.2 Zirconium Phosphate 42
4.2.3 MCM-41 Silica Grafted Titanium Alkylphosphates 44
4.2.4 Hybrid Titanium Butylphosphates 48
4.3 Column Study 52
4.3.1 Amorphous Titanium Phosphate 52
4.3.2 α-Zirconium Phosphate 53
5 Conclusions and Outlook 55
References 58

1 Introduction

1.1 A Recap of the Rare-Earth Elements

By the official International Union of Pure and Applied Chemistry (IUPAC, 2015) definition, the *rare-earth elements* (REEs) consist of a group of 17 elements: scandium (Sc), yttrium (Y), lanthanum (La), cerium (Ce), praseodymium (Pr), neodymium (Nd), promethium (Pm), samarium (Sm), europium (Eu), gadolinium (Gd), terbium (Tb), dysprosium (Dy), holmium (Ho), erbium (Er), thulium (Tm), ytterbium (Yb) and lutetium (Lu).

The REEs have a Nordic origin. In 1794, Finnish chemist Johan Gadolin first recognised yttria (mixed yttrium oxide) from a mineral sample originated from Swedish village Ytterby. All together the discovery of seven REEs (Y, Er, Tb, Yb, Ho, Tm, Gd) can be traced back to the same geographical location. The REEs are not rare judged from their overall abundance in the Earth's upper crust (**Figure 1**), as they are considerably more abundant than the precious metals (e.g. gold, platinum). The only exception is Pm without no stable isotopes. A rhythmic alternation in abundance between elements of odd and even atomic number, the "zig-zag effect", arises from the stability difference of nuclei during cosmic synthesis.

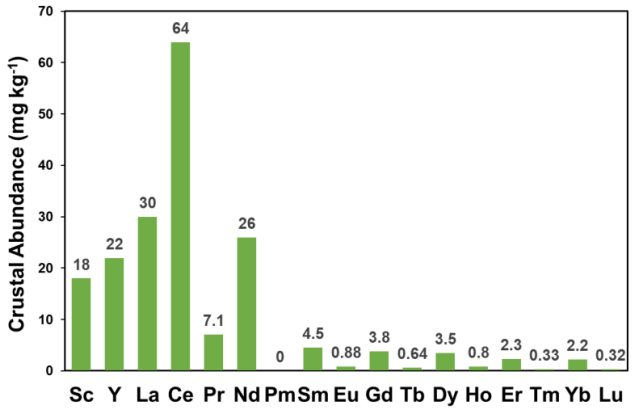


Figure 1. Crustal abundances of the REEs (data taken from Taylor and McClennan, 1985).

The term “rare-earth” is somewhat misleading. It is inherited from the historical difficulties in separating them from each other (“rare”) and that the REEs are stable in oxide form (“earth”).

Sc, first predicted by Dimitri Mendeleev in the periodic table as “eka-boron”, was discovered in 1879 by Swedish chemist Lars Nilson through analysing the Scandinavian minerals euxenite and gadolinite. This element with an atomic number of 21 is cosmically created by the rapid neutron-capture process in supernovae. Sc is the first transition metal and features a ground electron structure of [Ar] $3d^14s^2$. The most common oxidation state is +3 where the $3d^14s^2$ electrons are all lost. ^{45}Sc is the only stable and naturally occurring Sc isotope.

Y, with an atomic number of 39, is situated below Sc in the period table and named after the village Ytterby. The ground electron configuration of Y atom is [Kr] $4d^15s^2$ and it makes Y almost exclusively trivalent (+3). ^{89}Y is the sole stable Y isotope in nature. Radioactive ^{90}Y with a half-life of 64 h is extensively used for radiopharmaceutical purpose.

Table 1. Selected characteristics of lanthanide elements and ions.

Element	Symbol	Atomic number	Electron configuration of Ln^{3+}	Effective ionic radius (Shannon, 1976) of 6-coordinated Ln^{3+} (pm)	Possible oxidation state(s)	Colour of Ln^{3+} in solution
Lanthanum	La	57	[Xe]	103.2	+3	Colourless
Cerium	Ce	58	[Xe] $4f^1$	101.0	+3, +4	Colourless
Praseodymium	Pr	59	[Xe] $4f^2$	99.0	+3, +4	Yellow-green
Neodymium	Nd	60	[Xe] $4f^3$	98.3	+3, +4	Violet
Promethium	Pm	61	[Xe] $4f^4$	97.0	+3	Pink
Samarium	Sm	62	[Xe] $4f^5$	95.8	+2, +3	Yellow
Europium	Eu	63	[Xe] $4f^6$	94.7	+2, +3	Colourless
Gadolinium	Gd	64	[Xe] $4f^7$	93.5	+3	Colourless
Terbium	Tb	65	[Xe] $4f^8$	92.3	+3, +4	Pale pink
Dysprosium	Dy	66	[Xe] $4f^9$	91.2	+3, +4	Yellow-green
Holmium	Ho	67	[Xe] $4f^{10}$	90.1	+3	Yellow
Erbium	Er	68	[Xe] $4f^{11}$	89.0	+3	Pink
Thulium	Tm	69	[Xe] $4f^{12}$	88.0	+2, +3	Green
Ytterbium	Yb	70	[Xe] $4f^{13}$	86.8	+2, +3	Colourless
Lutetium	Lu	71	[Xe] $4f^{14}$	86.1	+3	Colourless

Lanthanides, alternatively *lanthanoids*, are a part of the group 3 and f-block elements ranging from La to Lu. They are formed by gradually filling the 4f electron

shell. Some of the key physicochemical properties of lanthanide and lanthanide ions (Ln^{3+}) are summarised in **Table 1**.

Both the chemical resemblance and the distinctive physical properties of the lanthanides are resulted from the fundamental electron configurations of the lanthanide atoms/ions. The 4f electrons are not accommodated in the outermost electron shell and they are perfectly shielded by the $5s^2 5p^6$ electrons with larger radial extension (see for example the Harteww-Fock calculation results of Gd^+ in **Figure 2**). The size of Ln^{3+} decreases from La^{3+} to Lu^{3+} because of the increase in nuclear charge, and this is known as the *lanthanide contraction*. The shielded 4f electrons hardly ever participate in bonding and therefore the chemical behaviour of Ln^{3+} ions are similar. Despite the similarity, the properties of Ln^{3+} experience discontinuity at quarter, half, three-quarter and complete filling of the 4f electron shell (McLennan, 1994). This effect—*the tetrad effect*—divides the lanthanides into four subgroups: La—Nd, Pm—Gd, Gd—Ho and Er—Lu, with Gd being an element common to the two central tetrads (Peppard et al., 1960).

Lanthanides show very diverse physical characteristics, enabling them for a range of magnetic and optical applications. The embedded 4f electrons maintain distinctive elemental properties because they are highly localised. As a result, complex magnetic properties stem almost solely from the motion of 4f electrons and they are not easily affected by the matrix. The intra-4f transitions result in long life-time optical emission that falls in the window for many applications (Digonnet and Dekker, 2001).

No consensus has been reached regarding the classification of the REEs. In general, the REEs are allocated into either two subgroups (light and heavy REEs) or three subgroups (light, medium and heavy REEs). The underlying reasons for splitting them into groups are arguably the differences in chemical behaviour and the occupation of the 4f electron shell. Hence, most often the dividing line for light and heavy REEs lies near Eu or Gd. Similar situation applies for the definition of light and heavy lanthanides.

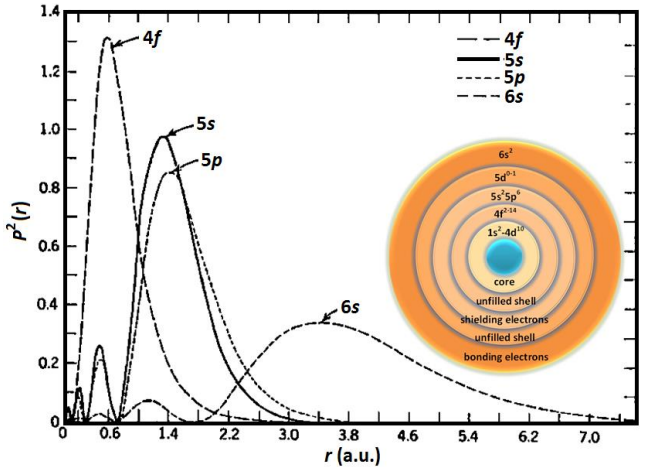


Figure 2. Square of the radial wave functions for the 4f, 5s, 5p and 6s energy levels in Gd^+ (Freeman and Watson, 1962; Rivera et al., 2012). *Reproduced with permission from the American Physical Society.*

Sc does not suit in such light-heavy classification because of its rather different properties. Y, however, is almost always regarded as a heavy REE due to its chemical resemblance to Dy and Ho. More discussions regarding the different classifications adopted by IUPAC and the European Union (EU) are available elsewhere (Binnemans et al., 2018).

In this dissertation, the light REEs are defined as from La to Eu and the heavy REEs from Gd to Lu, following the IUPAC recommendation.

1.1.1 Natural Occurrence and Deposits

All REEs are lithophile elements, meaning that they predominantly bond with oxygen and are naturally present in the forms of oxides, carbonates, silicates or phosphates (Taylor and McLennan, 1981). Owing to the great chemical similarities, hardly ever does one REE occur without other REEs in the same mineral.

The most important mineable rare-earth minerals are monazite, bastnäsite, xenotime and ion-adsorption clays. Light REEs are often hosted in monazite [(Ce, La, Y, Th)PO_4] and bastnäsite [(Ce, La)$(CO_3)F$], whereas heavy REEs occur in xenotime (YPO_4) and ion-adsorption clays (aluminosilicate minerals). The mineralogy of the REEs are complex and explained in detail by Henderson (1984).

Globally, there are about 34 countries that have REEs reserves (Chen, 2011). **Table 2** lists the worldwide reserves and mine production of REEs in 2016 and 2017

(U.S. Geological Survey, 2018). The world's largest REE deposit at Bayan Obo, Inner Mongolia, China, accounts for the majority of world REE supply since the 1980s. Another well-known deposit is located in Mountain Pass, California, United States, which was reopened in 2012 but again put on care-and-maintenance status since late 2015.

Table 2. World REEs mine production and reserves (in metric tonnes of rare-earth oxides). Reproduced with modification from U.S. Geological Survey (2018).

Country	Mine production		Reserves
	2016	2017	
Australia	15,000	20,000	3,400,000
Brazil	2,200	2,000	22,000,000
Canada	—	—	830,000
China	105,000	105,000	44,000,000
Greenland	—	—	1,500,000
India	1,500	1,500	6,900,000
Malawi	—	—	140,000
Malaysia	300	300	30,000
Russia	2,800	3,000	18,000,000
South Africa	—	—	860,000
Thailand	1,600	1,600	NA
United States	—	—	1,400,000
Vietnam	220	100	22,000,000

1.1.2 Applications and Criticality

REEs have found a wide range of applications since 1900s. In early years, when obtaining individual REE was not feasible, misch metal (an alloy of rare-earth metals including mostly Ce, La, Nd) was used as a spark source to start fire as well as in steel-making to improve mechanical properties. Nowadays, REEs have become increasingly vital to modern technologies, especially for improving energy efficiency. **Figure 3** provides an overview of the usage of REEs. The most important applications are catalysts (La and Ce for petroleum cracking; Ce for automotive catalytic converter), permanent magnets (Nd, Dy and Pr for neodymium-iron-boron magnets; Sm for samarium-cobalt magnets) and lamp phosphors (Y, Eu). The use of REEs in permanent magnets is forecast to increase over the next decade due to the shifting from internal combustion engine vehicles to hybrid and electric cars (Roskill, 2016).

In the case of Sc, applications have been limited because of its low availability and high price. According to U. S. Geological Survey (2017), the price of Sc oxide with a purity of 99.99% stood at approximately 5 USD per gram (5-kg lot size). Aluminium-Sc alloys provide excellent strength and stability, which are now applied in aerospace industry and high-end sports equipment. Solid oxide fuel cells utilising Sc stabilised zirconia consume another major part of Sc (Badwal et al., 2000). Nevertheless, the global Sc production is considered to be lower than 20 tonnes per year in terms of Sc_2O_3 (Ricketts et al., 2018). The estimation is questionable because in many countries trading Sc is regarded as a secret due to its use in manufacturing military aircrafts.

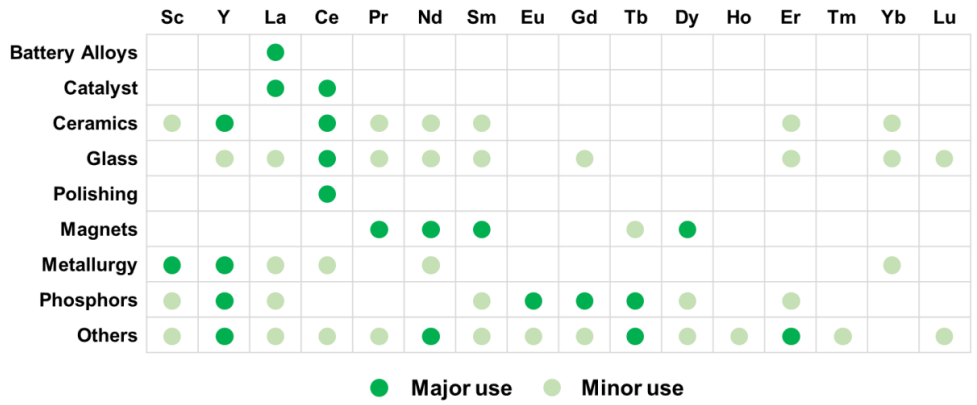


Figure 3. Summary of qualitative use for REEs. Reproduced with modifications from Zepf (2013).

REEs are raw materials that are crucial to Europe's economy. They are closely linked to many industries across the supply chain stages, they constitute the basis of many modern electronic devices and they are irreplaceable components in clean technologies. The supply of REEs are dominated by China, the United States and Russia, which altogether accounts for 99% of the EU imports. In general, there is no manufacturing activity within the EU. Consequently, the REEs have been identified as critical raw materials (CRMs) by the EU in all of its three CRM reports published in 2011, 2014 and 2017 (European Commission, 2017).

1.1.3 Technosphere Mining

The high criticality of the REEs has triggered a search for alternative supply routes in conjunction to primary mining. The term *technosphere mining* arose from similar initiative (Johansson et al., 2013). In general, the accumulation of REEs within the technosphere can be categorised into *active* and *inactive stocks*. On one hand, the active stock involves all REEs-containing goods that is being used or circulating in the society. At the end of their product lifetime, recycling and reprocessing are considered as efficient methods for technosphere mining. On the other hand, the inactive stock refers to unwanted wastes. REEs are present, though not in high concentrations, in a multitude of industrial process residues, e.g. phosphogypsum, mine tailings, metallurgical slags and wastewater streams (Binnemans et al., 2015). Considering the vast volume of these inactive stocks, significant amount of REEs can be mined. The dissertation work is initiated to contribute to the technosphere mining of REEs in the case of bauxite residue.

1.2 Bauxite Residue: A Waste or Resource?

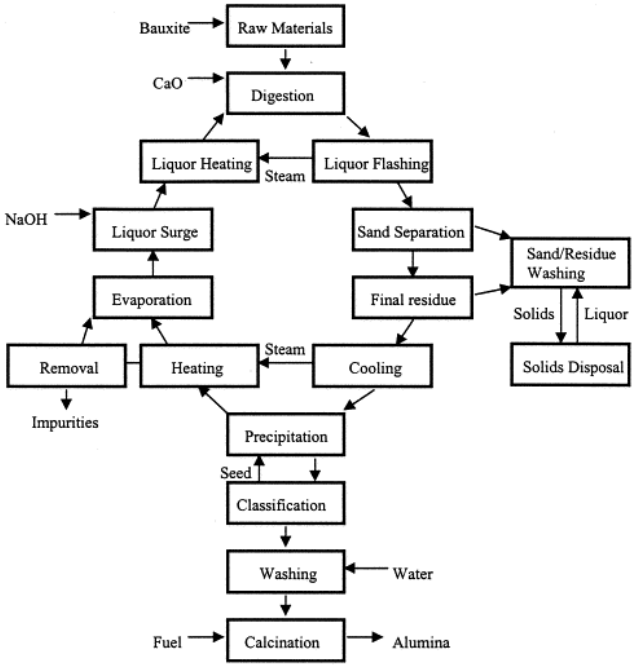


Figure 4. The Bayer process. *Reproduced from Hind et al. (1999) with permission from Elsevier.*

Globally speaking, the *Bayer process* is the most widely applied industrial process for the production of alumina since the late nineteenth century. It is named after its inventor Karl Bayer in 1887. In the cyclic Bayer process, aluminium-containing mineral ores are hydrothermally digested by caustic soda and alumina is subsequently precipitated through a seeding method (**Figure 4**).

Bauxite is the principle aluminium ore used in the Bayer process. It is a type of sedimentary rock which contains a relatively high content of aluminium minerals, such as gibbsite [$Al(OH)_3$], boehmite [γ-AlO(OH)] and diaspore [α-AlO(OH)] (Bogatyrev et al., 2009). Notably, bauxites also contain other minerals that are not recovered through the Bayer process: hematite (Fe_2O_3), goethite [FeO(OH)], quartz (SiO_2), titanate (TiO_2, rutile or anatase), etc. There are more than 100 operating Bayer alumina plants worldwide, producing some 126 million tonnes of alumina in 2017 (International Aluminium Institute, 2018). The global annual growth rate of aluminium demand is projected to be 6% (International Aluminium Institute, 2015).

Bauxite residue (BR), often referred by the public as “red mud”, is the slurry waste generated by the Bayer process. The characteristic red colour of BR results from its high iron content. High alkalinity is the most important feature of BR, with a typical pH range of 10—13. The BR composition varies according to the original bauxite source and the digestion protocol. An estimated concentration range of major components in BR is listed in **Table 3**.

Table 3. Chemical composition range (%) for the BR main components. Data taken from International Aluminium Institute (2015).

Component	Fe_2O_3	Al_2O_3	TiO_2	CaO	SiO_2	Na_2O
Range (%)	20—45	10—22	4—20	0—14	5—30	2—8

Apart from the major components, BR hosts a wide range of minor and trace-level metallic elements as well as organic compounds. Elements such as arsenic, beryllium, cadmium, chromium, copper, gallium, lead, manganese, mercury, nickel, potassium, vanadium and zinc are present in certain type of BR.

Bauxite, as a mineral, is classified into naturally occurring radioactive material (NORM) due to the presence of U and Th and their decay chains. Most of these radioisotopes are un-dissolved throughout the Bayer process and end up enriched in BR. A typical concentration for ^{238}U in BR is from 0.08 to 0.66 Bq g^{-1}, whereas for ^{232}Th is from 0.07 to 1.8 Bq g^{-1} (International Aluminium Institute, 2015). Valorising BR in large quantity must meet the required NORM legislations.

1.2.1 Disposal, Storage and Remediation

Globally, alumina is produced along with the stockpiling of BR. The weight ratio of BR to alumina product is about 1 to 1.5 (Kumar et al., 2006), translating into an annual world production of BR at 150 million tonnes (Evans, 2016). Combined with the legacy BR sites, it is estimated that the total world BR inventory stands at some 3 to 4 billion tonnes.

Marine discharge was the simplest and first method for BR disposal. The BR slurry is discharged directly into the deep ocean via a pipeline. Obviously the highly alkaline slurry would induce a negative environmental impact, and marine discharge is not practiced anymore. Historically, when the alumina plant was not geographically close to the sea, lagooning was used as a BR disposal method. The BR slurry was pumped into land-based ponds for storage. One of the most important disadvantage of lagooning is the low solid content of BR, and this was tragically demonstrated by the Ajka accident in Hungary, October 2010. Following the collapse of a containment structure, about 700,000 m^3 of BR slurry flooded around 40 km^2 of agricultural area, causing ten fatalities and severe environmental pollution (Gelencsér et al., 2011).

Dry stacking and dry cake disposal have subsequently been the major BR disposal methods. BR is mechanically de-liquored (e.g. by a filter press) to a paste or cake and then stacked in storage area. The characteristics of the dry cake reduces the potential of environmental hazard and broadens the option for rehabilitation and reuse (Power et al., 2011). Efforts have been made in remediating and rehabilitating BR disposal area by capping with soil layer or gypsum.

1.2.2 Rare Earth Contents in Bauxite Residue

Stockpiled BR is generally considered as a waste. Till now, industrial scale valorisation of BR only happens in cement, steel and construction industry. Less than 3% of bauxite residue produced annually is used in a productive way (Evans, 2016). However, considering the technosphere mining concept, BR would be a potential candidate for metal recovery. Based on **Table 3**, iron, aluminium and titanium recovery from BR seem viable through certain pyrometallurgical and/or hydrometallurgical approach (Liu et al., 2014). However, the hidden value of BR is not only represented by the major metals, it is also reflected in trace-level valuable metals such as the REEs.

REEs are not digested by the Bayer process and they are subsequently concentrated by a factor of 2 in the BR, compared to the original bauxite. The REEs content in the BR depends largely on the source bauxite, with karst bauxite hosting more REEs than lateritic bauxite. **Table 4** lists the typical REEs contents in Greek karst bauxite, Ghana lateritic bauxite and BR produced from a mixture of these two bauxites (4:1 weight ratio) in the Bayer alumina plant of Aluminium of Greece.

Table 4. Content of REEs (mg kg^{-1}) from bauxites and BR. Reproduced from Vind et al. (2018a and 2018b) under the CC BY 4.0 licence. Standard deviations are omitted here, and N.D. means not detected.

Element	Greek karst bauxite	Ghana lateritic bauxite	BR
La	58	19.1	130
Ce	206	34	480
Pr	15	N.D.	29
Nd	53	13	107
Sm	9.8	2.0	19.4
Eu	2.4	0.8	4.6
Gd	10.6	N.D.	22.0
Tb	2.3	<0.5	3.3
Dy	9.8	N.D.	20.1
Ho	2.1	N.D.	4.1
Er	7.2	N.D.	13.3
Tm	<2	N.D.	<2
Yb	7.0	2.5	13.8
Lu	<2	0.4	2.2
Total Ln	382.3	71.8	854.4
Sc	42.4—52.8	8.6	97.6
Y	48	N.D.	108

The REE-related mineralogical phases of BR have recently been recognised by Vind et al. (2018a and 2018b) through a combination of microanalyses. Light REEs are predominantly present in the form of ferrotitanate (REE,Ca, Na)(Ti,Fe)O_3, whereas their heavy counterparts are found in yttrium phosphate phases (xenotime and churchite). Sc is mainly hosted in hematite, which does not dissolve in the Bayer liquor.

BR can be considered as a rich reservoir for REEs and it might be a partial solution to decrease the REEs supply risk in the EU. In the case of the Greek BR, Sc with the concentration of up to 100 mg kg^{-1} is particularly interesting. Due to its high price, Sc alone accounts for more than 95% of the economic value of the total REEs in BR (Binnemans et al., 2015).

1.2.3 Near-Zero-Waste Valorisation of Bauxite Residue

BR is, after all, an industrial waste with large volume and harsh physicochemical properties. Simply recovering minor metal components cannot be a viable option. Large-scale valorisation of BR could only be possible with an integrated flowsheet to recovery all valuable metals and to reduce the overall waste volume. A combination of pyrometallurgical methods (smelting, roasting, etc) are proposed for the recovery of major metal elements from BR, namely Fe, Al and Ti (Borra et al., 2016). The resultant slag is enriched in REE and can be applied for hydrometallurgical leaching and separations. The final REE-depleted residue would possibly be tuned for application in building materials and cementitious binders (Pontikes and Angelopoulos, 2013). The dissertation work falls within the framework of a near-zero-waste valorisation of BR, where the REEs recovery would enhance the profitability of such flowsheet and in the meantime provide an alternative route for REEs mining.

1.3 Hydrometallurgical Separation and Recovery of Rare-Earth Elements

Hydrometallurgy is a branch of metallurgy that conducts extraction and separation of metals utilising aqueous solution based chemical methods. The

separation of REEs are mainly achieved by hydrometallurgical techniques, both in laboratory and in industrial scale. REE-bearing ores or residues are usually first leached by acids and the dissolved metal ions are separated through precipitation, solvent extraction and/or ion-exchange processes. The obtained pure REE-containing fractions are further subject to precipitation and electrochemical methods (electrowinning and electrorefining) for the recovery of metal compounds and metals.

1.3.1 Acid Leaching

Filter-pressed BR is still highly caustic, hence large amounts of acid are needed to compensate the alkalinity and then to dissolve the minerals during the leaching process. Mineral acids including hydrochloric acid (HCl) and sulphuric acid (H_2SO_4) are typically used for acid leaching due to their lower price compared to organic acids, though the later (e.g. citric acid) can be more selective for dissolving REEs (Borra et al., 2015).

Ideally, a leaching process should provide a maximum amount of REEs dissolution and a minimum amount of other metal leaching. In the case of BR, the major obstacle hampering the downstream REE separation are the dissolution of Fe and Al minerals. The selection of leaching process needs to find a balance point between REEs recovery and major metal dissolution. Moreover, in practical conditions, the dissolution and supersaturation of silica lead to silica gel formation. The silica gel solutions can no longer be filtered and significantly decrease the leaching kinetics (Queneau and Berthold, 1986). Dry digestion followed by water leaching (Marin Rivera et al., 2018) and cooperative leaching in hydrogen peroxide and sulphuric acid media (Alkan et al., 2018) are shown to perfectly inhibit the silica gel formation.

Even under optimised conditions, the *pregnant leaching solution* (PLS) of BR features REEs in mg L^{-1} scale and major metals (Fe, Al, Ti, Ca) in g L^{-1} scale. Due to the big concentration difference, complicated downstream processing is necessary for trace metal recovery.

1.3.2 Selective Precipitation

One of the simplest yet effective PLS pre-treatment methods is selective precipitation. Different metal ions start to precipitate in the form of hydroxides under different solution pH. From theoretical calculations (**Figure 5**), thermodynamically the complete group separation of REEs from PLS is achievable by simple sodium hydroxide (NaOH) addition. However, in reality co-precipitation hinders the process as REE ions are captured into the crystals of iron(III) hydroxide when Fe^{3+} starts to precipitate.

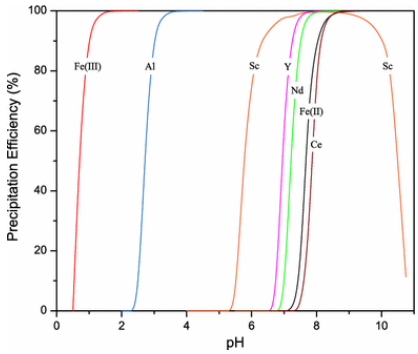


Figure 5. Visual MINTEQ simulation for hydroxide precipitation from red mud leachate (sulphuric acid). *Reproduced from Yagmurlu et al. (2017) with permission from Springer Nature.*

Yagmurlu et al. (2017 and 2018) proposed a multi-stage precipitation route for the pre-treatment of BR PLS, where the majority of the Fe^{3+} is first removed by ammonia (NH_4OH) and then the REE ions by phosphate precipitation. The obtained solids are favourable for further processing since the REE-to-Fe ratio is significantly improved compared to that in the PLS.

REEs can be selectively precipitated as sodium double sulphate salts (Kul et al., 2008). The reaction is expressed in Eq. 1.

$$REE_2(SO_4)_3 + Na_2SO_4 + 2H_2O \rightarrow Na_2SO_4 \cdot REE_2(SO_4)_3 \cdot 2H_2O \quad \text{(Eq. 1)}$$

The double sulphate precipitation is particularly useful since the reaction happens even at acidic pH, thereby avoiding the co-precipitation of Fe^{3+}. Pietrelli et al. (2002) stated that the solubility of such double sulphate salts is extremely low. Despite such claim, the solubility is not low enough to warrant REE recovery from dilute streams. For example, the solubility of $NaLa(SO_4)_2$ is reported as 2.34 g L^{-1} (Porvali et al., 2018), and for Sc, the residual Sc concentration after $NH_4Sc(SO_4)_2$ or

$(NH_4)_3Sc(SO_4)_3$ precipitation is about 10 mg L^{-1} at 60 °C (Pasechnik et al., 2017 and 2018).

1.3.3 Solvent Extraction

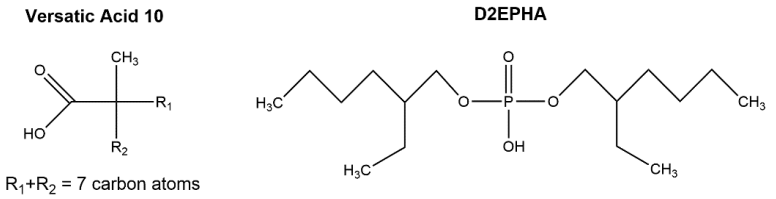
Solvent extraction (SX), also known as liquid-liquid extraction, utilizes a bi-phasic system for selectively separating metal ions. An aqueous phase containing metal ions are put in contact with an organic phase containing extractants. After mixing, the two immiscible phases are let settle and certain metal ions are enriched in one of the phases. Depending on the complexity of the PLS, multi-stage SX systems requires loading, scrubbing, stripping and regeneration steps that need to be designed on a case-by-case basis. Repeating the scrubbing and/or selective processes results in obtaining purer metal fractions.

The core of any SX system is essentially the extractant. The structure of an extractant governs the separation mechanism and subsequently the selectivity.

Acid extractants behave as cation exchangers for metal uptake and the extraction follows Eq. 2. Carboxylic acids, phosphorus acids (including phosphoric, phosphonic and phosphinic acids) and sulphonic acids belong to this group. The structure of some common extractants from this group are illustrated in **Scheme 1**.

$$\mathrm{M}^{n+} + n\overline{\mathrm{HA}} \leftrightarrow \overline{\mathrm{MA}_n} + n\mathrm{H}^{+} \qquad \text{(Eq. 2)}$$

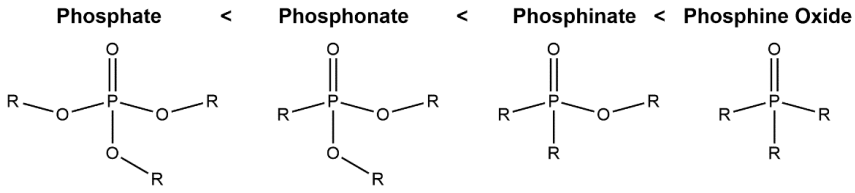
where M^{n+} represents metal ion with an n+ charge, HA is the acid extractant and the barred components are in the organic phase.



Scheme 1. Chemical structure of two representative acid extractants, versatic acid 10 and bis(2-ethyl)hexyl phosphoric acid (D2EPHA).

Solvating extractants extract neutral metal complexes by electron-donating solvation. The most important solvating extractants are alkylphosphates, phosphonates and phosphinates and phosphine oxides. The electron density of the phosphoxyl group decreases from phosphine oxides to phosphates, and so does their bonding strength with metals (Scheme 2). Tri-*n*-butyl phosphate (TBP) is widely used for extraction and separation of the REEs. The extraction in nitrate medium follows Eq. 3.

$$\mathrm{REE^{3+}} + 3\mathrm{NO_3^-} + 3\overline{\mathrm{TBP}} \leftrightarrow \overline{\mathrm{REE(NO_3)_3(TBP)_3}} \qquad \text{(Eq. 3)}$$



Scheme 2. Chemical structure of phosphorus-based solvating extractants and the trend in their bonding strength with metals.

Besides these two types of extractants, *chelating extractants* employing coordination functional groups have been studied (Xie et al., 2014; Wang and Cheng, 2011).

One of the major drawbacks of SX is the organic volatility. The extractants are usually diluted by organic solvent such as kerosene. In large scale application, the volatile organic compounds are difficult to handle and pose occupational hazard.

1.3.4 Ion-Exchange

The ion-exchange separation of REEs was intensively studied during the Manhattan project. Through a combination of organic resin and complexing elution solution, individual lanthanides were separated for analytical purpose (Tompkins et al., 1947). Versatile organic resins were later developed, mainly on top of the backbones of styrene and acrylics (Lucy, 2003). Ion-exchange process with organic resins is now only used for producing small amounts of high-purity REEs. The ion-exchange separation of REEs on purely inorganic materials remain largely unexplored.

1.3.5 Recovery methods

To obtain the technologically useful final products, the dissolved REE cations need to be converted to REE compounds or metals. Oxalic acid precipitation is the most applied route for REE recovery from aqueous solution (Bandara et al., 2016). REE oxalates [$(REE)_2(C_2O_4)_3$] are insoluble precipitates that, upon calcination, convert directly to oxides. Oxalic acid solution can be directly used for elution from IX column (Tompkins et al., 1947) and for stripping in SX process (Jorjani and Shahbazi, 2016). Some industrial processes utilise carbonate or sulphate precipitation for REE recovery (Xie et al., 2014). Following the production of pure REE compounds, REE metals are produced via molten salt electrolysis, namely electrowinning and electrorefining processes (Tunsu et al., 2015).

1.4 Metal(IV) Phosphate Materials

Oxygen atoms belonging to phosphate tetrahedra (PO_4) can be shared with metal(IV) in an octahedral configuration, giving rise to a number of metal(IV) phosphate materials with vastly different structure and morphology (Alberti et al., 1996). Amongst all the metal(IV) phosphate materials, amorphous ones have been intensively studied during 1955—1965, particularly for their use as inorganic ion-exchangers at elevated temperature and radiation doses. The first crystalline type, α-layered zirconium phosphate (ZrP), was prepared in 1964 by Clearfield and Stynes (1964). Since then, ZrP and its analogue titanium phosphate (TiP) have been extensively investigated. They are used for ion-exchange, catalysis as well as ionic conducting materials. The structure of two most typical kinds of layered ZrP materials are illustrated in **Figure 6**. Compared to silica materials, the acid stability of metal(IV) phosphate is a prominent advantage.

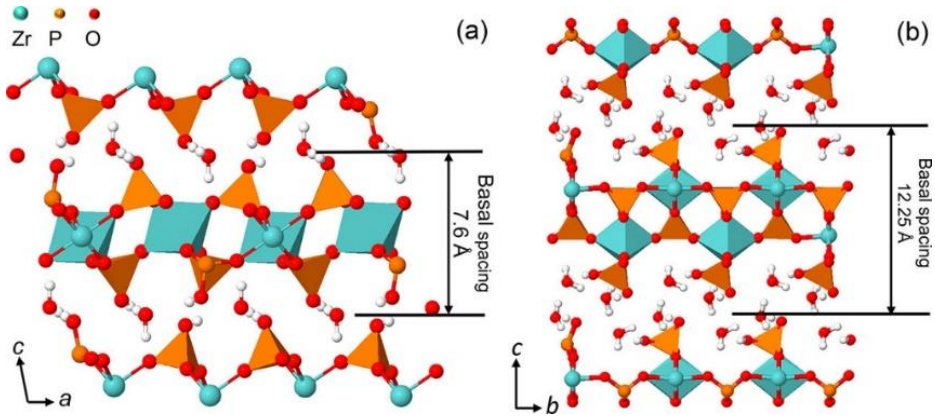


Figure 6. Structures of (a) α-ZrP and (b) γ-ZrP**.** *Reproduced from Cheng, et al. (2018) with permission from the American Chemical Society.*

1.4.1 Titanium Phosphate Materials

The aqueous chemistry of titanium(IV) is extremely limited due to its low solubility at practically all pH. Titanium(IV) is only soluble in highly acidic media or when chelating agents are present. Only through acid reflux or hydrothermal route, one may obtain crystalline TiP materials from aqueous precursors.

Directly contacting titanium(IV) and phosphate solution instantly produces highly insoluble amorphous TiP precipitates. Upon prolonged refluxing or hydrothermal treatment in phosphoric acid, the amorphous phase crystallises. Three most important crystalline phases for TiP materials are, namely, α-, β- and γ- phases. Notably, these phases are all in lamellar formats where the layers stack upon each other via Van der Waals forces. The layers are formed by titanium atoms in a plane bridged by the oxygen atoms in phosphate groups which are located above and below the plane. The distribution of phosphate groups therefore creates porous zeolitic cavities. The key structural information of these layered TiP materials is summarised in **Table 5**. The different phosphate groups are distinguishable through the solid-state ^{31}P NMR technique. Andersen et al. (1998a) studied the formation regions of different TiP materials (**Figure 6**). Higher refluxing temperature and more concentrated phosphoric acid favour the formation of β- and γ-TiP, where β-TiP is the fully dehydrated form of γ-TiP.

Table 5. Selected parameters of layered TiP materials.

Formula	Unit cell parameters				Interlayer distance (Å)	Free area ($Å^2$)	Ion exchange capacity (mequiv g^{-1})	Ref.
	a (Å)	*b* (Å)	*c* (Å)	*β* (°)				
α-$Ti(HPO_4)_2 \cdot H_2O$	8.630	5.006	16.189	110.2	7.56	21.6	7.76	Christensen et al, 1990
β-$Ti(PO_4)(H_2PO_4)$	18.950	6.313	5.139	105.37	9.14	-	-	Andersen et al., 1998a
γ- $Ti(PO_4)(H_2PO_4) \cdot 2H_2O$	5.181	6.347	11.881	102.59	11.60	16.5	7.25	Christensen et al, 1990

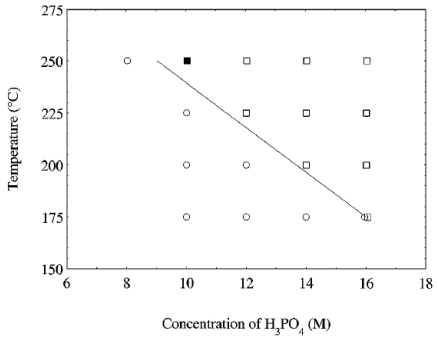


Figure 6. Formation regions of α- and β-/γ-TiP (no distinction is made between β- and γ-TiP). ○, α-TiP powder; □, γ-TiP powder; ■, large γ-TiP crystals. *Reproduced from Andersen et al. (1998a) with permission from Elsevier.*

The composition of amorphous TiP (am-TiP) is not as clear as its crystalline counterparts. The types of ion-exchange groups found in am-TiP include $–HPO_4$ and $–H_2PO_4$, and very often a mixture of both. A recent article by Trublet et al. (2018) discussed the synthesis conditions of amorphous TiP materials. It appears that the amorphous nature may be related to greater surface area and higher ion-exchange capacity.

1.4.2 Ion-Exchange and Intercalation

Take α-TiP as an example, the α-type layers host $–HPO_4$ groups both above and underneath the Ti-oxo layers. The –OH groups pointing towards the interlayer cavities are ideal ion-exchange sites for cation uptake and for hosting basic organic molecules (such as amines). According to calculations, the α-layer theoretically permits the diffusion of spherical particles with a size of 2.61Å (Suarez et al., 1984a). The porous zeolitic nature of the crystals and the weak forces holding together the layers are the basis for ion selectivity and the expansion of the interlayer space during the intercalation process (Clearfield and Smith, 1969).

The ion-exchange behaviours of alkali and alkaline earth metal ions on layered metal(IV) phosphates have been well studied and understood already in the last

century. Numerous reports dealt with the intercalation of various amines and organic ammonium hydroxides into metal(IV) phosphate layers. A combination of titration, X-ray diffraction and calorimetry was used for monitoring the layer expansion and reaction stoichiometry (Suarez et al., 1984b; Espina et al., 1998). However, there remains little to no reports regarding the ion-exchange of REEs on TiP materials. Recently, the lanthanide separation behaviour on purely inorganic ZrP materials was studied by our group (Xu et al., 2017 and 2018). There was shown that lanthanide ions are not able to diffuse in a large extent into the interlayer cavities of α-ZrP. Enlarging the basal distance by means of intercalation with *n*-propylamine significantly improved the uptake of Eu^{3+} on α-TiP (Garcia-Glez et al., 2017). However, the enhanced uptake resulted from the sacrifice of amine, therefore the regeneration became a difficult task.

1.4.3 Design and Functionalisation of the Materials

Metal(IV) phosphate materials, featuring a robust inorganic structure with the presence of active sites on the particle surface, are an ideal platform for designing specific functionalities (Pica, 2017; Pica et al., 2018). To fully utilise the ion-exchange sites of these materials, many synthetic approaches have been proposed.

The easiest way to utilise more ion-exchange sites is by *controlling the crystallinity* of the materials. The lower degree of crystallinity creates more defects and amorphous phases that, in some cases, significantly improves the diffusion (Llavona et al., 1989). Perfectly crystalline materials are also difficult for further intercalation (Sun et al., 2005 and 2009).

Synthetic creation of *multidimensional pore-channel systems* is another way of improving the accessibility of the ion-exchange sites. Three-dimensional TiP materials with open pore structures have been synthesised through organic templating routes (Ekambaram and Sevov, 1999; Bhaumik and Inagaki, 2001). Both cationic surfactants (Jones et al., 2000) and non-ionic surfactants (Li et al., 2006; Thieme and Schuth, 1999) are possible templates for the synthesis of mesoporous TiP materials. Under fine-tuned conditions, mesoporosity can be

created in the absence of organic templates (Chowdhury and Naskar, 2016; Wang et al., 2014). However, the low solubility and high hydrolysis rate of Ti(IV) hinder the reproducible preparation of mesoporous TiP and TiO_2. Hierarchically porous TiP monoliths were prepared by sol-gel route utilising the phase separation behaviour of polymers (Zhu et al., 2016) or through self-formation process even without surfactants (Ren et al., 2006).

Pillaring is one of the common post-synthetic modification approaches for layered materials. The idea here is to use vertical pillars to support the extended layer gallery spacing, leaving large spaces in the order of 10—12 Å between them (Clearfield and Roberts, 1988). For layered metal(IV) phosphates, pillaring is often done by first intercalating the layers with organic amines or metal cations. The expended layers thereafter accommodate the precursor of pillars. Inorganic polymeric cations (such as Keggin ion $[Al_{13}O_4(OH)_{24}\cdot 12H_2O]^{7+}$), silica (Jiao et al., 1998) and titania (Das and Parida, 2006) are typical pillars. Another type of pillars is organophosphorus compounds, diphosphonic acids with large spacer groups between two phosphorus atoms were used for pillaring (Silbernagel et al., 2016).

Other post-synthetic functionalisation methods include the formation of nano-composites (Wang et al., 2016; Li et al., 2014) and surface grafting of functional groups (Zhou et al., 2014 and 2015).

2 Aim of the Study

The dissertation work focuses on designing novel metal phosphate-based functional materials for selective separation of REEs, with BR leachate as a potential end-application. Traditional group 4 metal phosphate materials are used as they are for REE ion-exchange separation, and later as an acid-resistant platform for further functionalisation. Synthetic work is guided by the separation performance, with an ultimate goal of producing highly selective materials. In the meantime, synthetic alteration of the surface functionality of the materials might generate fundamentally different separation mechanisms. More attention is paid on materials chemistry and solution chemistry, instead of the real-world engineering perspective.

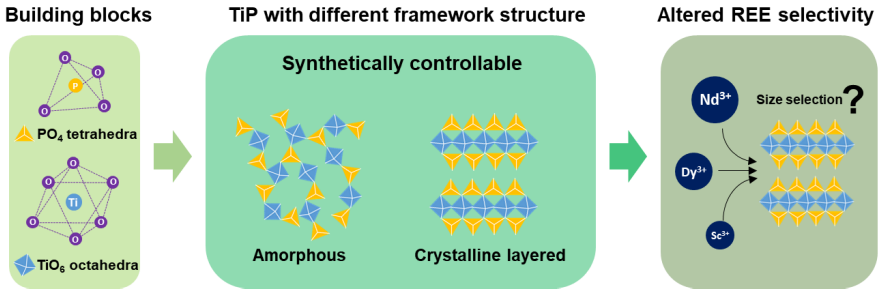
Three separation tasks relating to the recovery of REEs from BR are aimed within the framework of the dissertation, namely:

(1) Separation of REEs (especially Sc) from mineral matrix metals (e.g. Fe^{3+}), **articles I** and **II**;
(2) Separation of Sc from lanthanides, **article III**;
(3) Intralanthanide separation, **article IV**.

3 Experimental

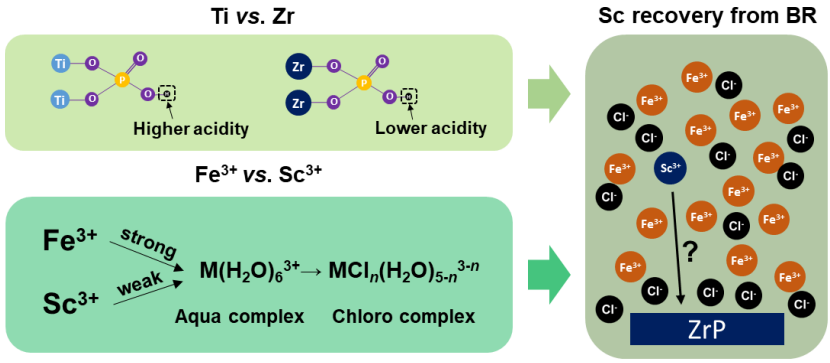
3.1 Experimental Design

Inorganic TiP materials with different framework structures were firstly studied for REEs separation in **article I** (**Scheme 3**). Namely, amorphous TiP, crystalline α-TiP and γ-TiP were selected. The synthesis routes for crystalline TiPs are well-established, however reproducibility issue remains in the synthesis of am-TiP. Hence, the characterisation of the products was investigated in detail. Both α- and γ- TiP feature layered 2D structure with different interlayer distances, which should create size-selection barrier for different metal ions upon entering. After screening for REEs selectivity with regards to mineral matrix metals, the most promising candidate was used for column separation trials using simulated BR leachate. Fe^{3+} was reduced on-column to Fe^{2+} to facilitate separation.



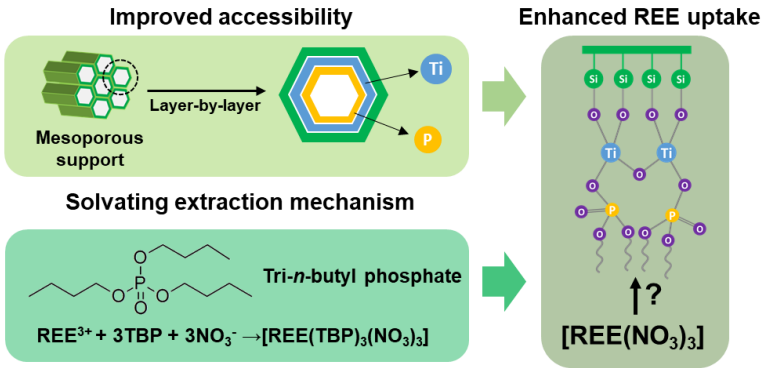
Scheme 3. Schematic illustration of the research idea tested in **article I**.

ZrP is an analogue of TiP. Zr^{4+} has lower charge density and therefore the acidity of hydrogenphosphate groups attached to Zr^{4+} is lower compared to those attached to Ti^{4+}. The acidity differences would result in an altered metal ion selectivity. In **article II**, crystalline α-ZrP material was studied for Sc^{3+} recovery from BR leachate with a special focus on the interfering Fe^{3+} (**Scheme 4**). Moreover, the addition of NaCl as a complexing agent to inhibit Fe^{3+} loading was studied. Fe^{3+} was not reduced by any means to Fe^{2+} in this experiment. Column experiments were run using real BR leachate samples for Sc^{3+} recovery.



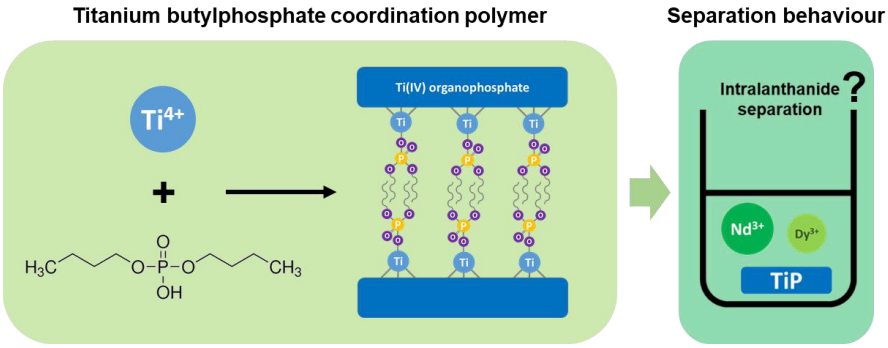
Scheme 4. Schematic illustration of the research idea tested in **article II**.

The initial idea behind using crystalline TiP or ZrP materials was to utilize the lamellar distance as an ion-sieve. However, it seemed that under acidic conditions relevant to the BR leachate, none of the REE ions were able to enter the interlayer cavity. Large amounts of the cation exchange sites inside the layers were not used and thus only a fraction of the capacity resulted in real uptake. To enhance the accessibility and surface area of the TiP materials, they were synthetically grafted onto mesoporous MCM-41 silica (**article III**). To further shift the extraction mechanism, short alkyl chains (n=2, 3 and 4) were later grafted on top of the TiP to mimic the structure of solvating extractants—tri-*n*-alkyl phosphate. The resulting materials were tested for Sc^{3+} separation from lanthanides as well as for intralanthanide separation.



Scheme 5. Schematic illustration of the research idea tested in **article III**.

To further increase the amount of titanium and alkylphosphate functional groups, as compared to **article III**, titanium alkylphosphate materials were directly synthesised by sol-gel reaction and their lanthanide separation behaviours were studied in **article IV**. The detailed separation mechanism and separation of adjacent lanthanide pairs were thereafter examined utilising a combination of kinetics study and characterisation methods.



Scheme 6. Schematic illustration of the research idea tested in **article IV**.

3.2 Materials Synthesis

3.2.1 Inorganic Metal(IV) Phosphates

The am-TiP synthesis was adapted from a precipitation route reported by Alberti et al. (1967). Both the α- and γ-TiP were hydrothermally synthesised in polytetrafluoroethylene-lined stainless-steel autoclaves. The α-TiP particles were grown from a gel-like precursor (Bao et al., 2011) and the γ-TiP was converted from the am-TiP phase (Andersen and Korby, 1998b). The precursors were prepared by titanium(IV) tetrachloride ($TiCl_4$) and ortho-phosphoric acid (H_3PO_4). The syntheses of TiPs are detailed in **article I**.

The α-ZrP was synthesized by a hydrothermal reflux method following the report by Sun et al. (2007) using zirconium oxychloride ($ZrOCl_2$) and H_3PO_4. The synthesis of ZrP is explained in **article II**.

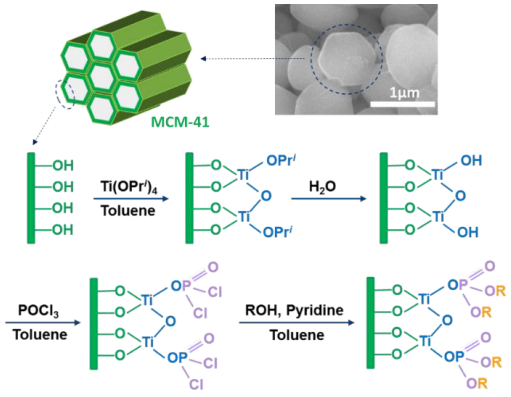
Note that to avoid high diffusional resistance and high surface physisorption, the materials were ground and sieved to a particle size of 74-149 μm (100-200 mesh) for further experiments.

3.2.2 MCM-41 Silica Grafted Titanium Alkylphosphates

The mesoporous support MCM-41 silica (M41) was synthesised according to a sol-gel template route (Cai et al., 1999). Tetraethyl orthosilicate was hydrolysed by ammonia solution under the presence of cationic surfactant hexadecyltrimethylammonium bromide. The surfactant was later removed by calcination in air.

Titanium alkylphosphates were grafted onto the surface of M41 through a layer-by-layer method utilising titanium(IV) isopropoxide ($Ti(OPr^{i})_4$) and phosphorus oxychloride ($POCl_3$) as a base-acid pair (Zhang et al., 2009), as demonstrated in **Scheme 7**. The reactive P—Cl bonds on the surface of the titanium modified M41 were later reacted with alcohol (ethanol, *n*-propanol or *n*-butanol) to obtain alkylphosphate groups, while the formed hydrochloric acid (HCl) is removed by forming pyridine complex. The detailed protocol can be found in **article III**.

The final products are denoted as M41-TiEtP, M41-TiPrP and M41-TiBuP corresponding to ethyl-, *n*-propyl- and *n*-butyl- grafted materials, respectively. For comparative reasons, the inorganic titanium(IV) phosphate grafted M41 (denoted as M41-TiP) was also synthesised.



Scheme 7. Synthesis route for M41 grafted titanium alkylphosphate materials. (R = H, Et, *n*-Pr and *n*-Bu).

3.2.3 Hybrid Titanium Butylphosphates

The hybrid titanium phosphate-butylphosphate (hybrid TiP) materials were prepared by precipitation in mixed inorganic-organic phosphate precursors. To enhance the solubility of the organic phosphate, a water-ethanol mixture was used as solvent for the synthesis. $TiCl_4$, H_3PO_4 and di-*n*-butyl phosphate (HDBP) were the starting chemicals. The P/Ti molar ratio in the synthesis liquors was fixed to 2 with a series of H_3PO_4-to-HDBP molar ratios (1:0, 3:1, 1:1, 1:3, and 0:1) varied. The obtained materials were denoted as TiP_x:y, where x:y is the H_3PO_4-to-HDBP molar ratio in the precursor. More details are provided in **article IV**.

3.3 Supporting Characterisations

3.3.1 Morphological and Compositional Characterisations

The morphology of the synthesised materials was observed on a Hitachi S-4800 field emission-scanning electron microscope (FE-SEM). The powder samples are stick to a carbon tape on an aluminium sample stage, and later coated with a few nm of Au-Pd film via sputtering to improve the surface conductivity.

The carbon (C) and hydrogen (H) contents of the materials were analysed by combustion followed by infrared spectroscopy for quantitatively determining the carbon dioxide (CO_2) and water. This is done on a Thermo Scientific Interscience Flash 2000 Elemental analyser (EA).

The contents of titanium (Ti) and phosphorus (P) were determined through total dissolution. The materials were digested in a mixture of HNO_3 and HF (or a mixture of H_2SO_4 and ammonium sulphate) in a CEM MARS 5 microwave digestion system. The concentrations of Ti and P were later measured by inductively coupled plasma-optical emission spectroscopy (ICP-OES) on a Perkin Elmer Optima 8300 equipment.

The thermogravimetry (TG) of the materials were studied either on a Mettler Toledo TGA/DSC 1 instrument, or, when it was necessary to analyse the evolved

gas, on a simultaneous TG/DSC apparatus (STA 449F3 Jupiter, Netzsch) connected to a JAS-Agilent gas chromatography-mass spectrometer (7890B GC/MSD5977A). Samples were heated under inert gas atmosphere (nitrogen or helium).

3.3.2 Structural Characterisations

First and foremost, the structure of the synthesised materials was examined by powder X-ray diffraction (XRD). The XRD patterns in the Bragg-Brentano geometry were recorded by a PANalytical X'Pert3 powder diffractometer equipped with a monochromatic CuKα radiation source (λ=1.54056 Å) operating at 40 kV and 40 mA. The powder samples were slurried in acetone and then dropped on a glass slide.

Vibrational spectroscopies including Fourier transform infrared spectroscopy (FTIR) and Raman spectroscopy were studied to gain insight into the functional groups. The IR spectra of the dried powders (650–4000 cm^{-1}) were recorded on a Perkin Elmer Spectrum One FTIR spectrometer equipped with a Universal ATR sampling accessory (with a germanium crystal). Raman spectra were recorded using a confocal Raman microscope (NTEGRA Spectra, NT-MDT) in the 100 to 1200 cm^{-1} region. The green 532-nm laser was generated from a Nd:YAG laser source with an output power of 20 mW. The samples for Raman measurements were prepared in a same fashion as the XRD samples.

The solid-state ^{13}C, ^{29}Si and ^{31}P magic angle spinning nuclear magnetic resonance (MAS NMR) spectroscopy of the materials were recorded to measure the chemical environment of the alkyl chain, silanol groups and the phosphate groups. Samples were packed into a 4-mm zirconia rotor and measured on a Bruker Avance III 500 MHz spectrometer. The ^{13}C spectra were acquired under ^{1}H-^{13}C cross-polarisation since ^{13}C is a weakly coupled nucleus. For ^{29}Si and ^{31}P spectra, a longer relaxation delay (100—200 s) was used. The spectra were externally referenced to adamantane (^{13}C), tetramethylsilane (^{29}Si) and 85% H_3PO_4 (^{31}P).

The porosity of the materials were determined by N_2 adsorption at 77 K, using a Quanta Chrome NOVA 2200e or a Micromeritics Tristar II Plus surface area and

pore size analyser. Samples were degassed in vacuum prior to analysis. The surface area was calculated by the Brunauer, Emmett and Teller (BET) method using the adsorption isotherms. Pore-size distributions were modelled by appropriate equations considering the pore-channel systems of the samples.

3.4 Separation Studies

3.4.1 Batch Experiments

The aqueous metal uptake by the synthesised materials was examined in a batch model solid-liquid system. Typically, a weighted amount of the solid material was placed in a 20-mL polyethylene vial and subsequently the metal-containing solution was introduced. The vials were constantly rotated on a rotary mixer (50 rpm) until the desired time was achieved. Aquilots of acids or bases (usually HNO_3 or NaOH) were added during the mixing to achieve certain solution pH. The solid and liquid separation was done either by centrifugation (in the case of inorganic materials) or by filtering through a 0.22 μm polyvinylidene fluoride syringe filter (in the case of hybrid materials). The metal concentration and the pH of the supernatant (or filtrate) were determined.

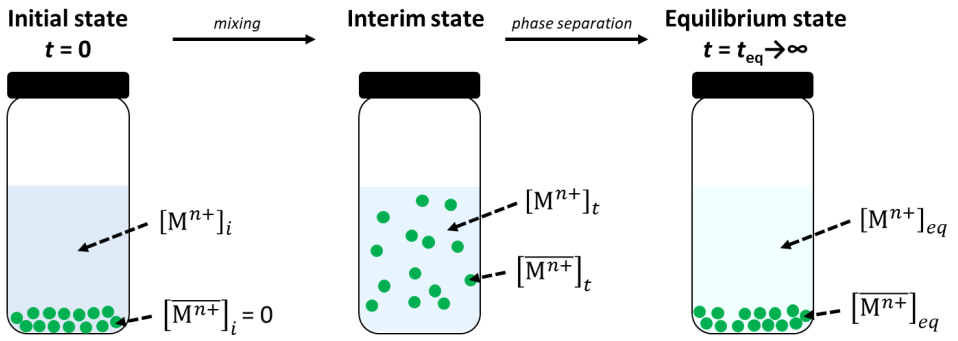
The aqueous solution was prepared by dissolving metal nitrate salts. In the batch experiments, single component, binary system and multi-component system were all involved depending on the experimental design. When investigating the solvating extraction mechanism, certain amount of salts was added to the solution to drive the extraction equilibrium.

The *equilibrium metal uptake* (q_{eq}, mg g^{-1}) shows the amount of metal in the solid phase at equilibrium according to Eq. 4. The unit of q_{eq} can be converted to mmol g^{-1} or mequiv g^{-1} to facilitate comparison between different metals.

$$q_{eq} = \left[\overline{\mathrm{M}^{n+}}\right]_{eq} = \left([\mathrm{M}^{n+}]_i - [\mathrm{M}^{n+}]_{eq}\right) \times \frac{V}{m} \qquad \text{(Eq. 4)}$$

where $\left[\overline{\mathrm{M}^{n+}}\right]_{eq}$ is the M^{n+} concentration in the solid (mg g^{-1}) in equilibrium state, $[\mathrm{M}^{n+}]_i$ and $[\mathrm{M}^{n+}]_t$ are respectively the M^{n+} concentration of the solution before and

after equilibration (mg L^{-1}), V is the volume of the solution (mL) and m is the mass of the material (g). The parameters are visually demonstrated in **Scheme 8**.



Scheme 8. Illustration of a single component batch solid-liquid sorption system and the notation of metal ion concentrations in different phases at different states.

The *distribution coefficient* (K_d, mL g^{-1}) demonstrates the distribution of a metal ion (M^{n+}) between the solid and the liquid phase (not necessarily at equilibrium). It is calculated by Eq. 5.

$$K_d = \frac{[\overline{M^{n+}}]_t}{[M^{n+}]_t} = \frac{[M^{n+}]_i - [M^{n+}]_t}{[M^{n+}]_t} \times \frac{V}{m} \qquad \text{(Eq. 5)}$$

where $[\overline{M^{n+}}]_t$ is the M^{n+} concentration in the solid (mg g^{-1}) after the sorption, $[M^{n+}]_t$ is the M^{n+} concentration of the solution after sorption (mg L^{-1}).

In binary or multi-component systems, the *separation factor* (*SF*, dimensionless) between two metals (M_1 and M_2) was calculated based on their K_d values following Eq. 6.

$$SF_{M_1/M_2} = \frac{K_d(M_1)}{K_d(M_2)} \qquad \text{(Eq. 6)}$$

The ion-exchange reaction stoichiometry can be verified by calculating the ratio of released H^+ to exchanged M^{n+} (Eq. 7).

$$H^+/M^{n+} = \frac{\Delta[H^+]}{\Delta[M^{n+}]} = \frac{10^{-pH_{eq}} - 10^{-pH_i}}{[M^{n+}]_i - [M^{n+}]_{eq}} \qquad \text{(Eq. 7)}$$

where pH_i and pH_{eq} are respectively the initial and equilibrium solution pH. The value of H^+/M^{n+} equals n if the exchanged ions exist in unhydrolysed form within the ion exchangers.

In some cases, batch elution experiments were conducted. After loading the solid materials with desired metal ions, phase separation was achieved by centrifugation and the remaining solid was washed repeatedly with appropriate solution to remove unbound metal ions. The wet materials were later dried in an oven before contacting with elution acids. After elution equilibrium, the metal concentration in the liquid phase was measured and used for calculation.

The $K_{d.elu}$ (mg L^{-1}) values of the elution systems were calculated as follows:

$$K_{\mathrm{d}.elu} = \frac{q_{elu.eq}}{c_{elu.eq}} = \frac{q_{eq} - c_{elu.eq} \times \frac{V}{m}}{c_{elu.eq}} \qquad \text{(Eq. 8)}$$

where q_{eq} and $q_{elu.eq}$ are the amount of metal uptake during loading and elution (mg g^{-1}) and $c_{\mathrm{elu.eq}}$ is the equilibrium concentration of metal in the elution acid (mg L^{-1}).

The metal concentrations were measured by an Agilent MP 4200 microwave plasma-atomic emission spectrometer (MP-AES) equipped with an SPS 3 auto-sampler. The detection limit of different elements falls within the range of 1—10 µg L^{-1}. The method provides almost identical analysis results compared to inductively coupled plasma-mass spectrometry (ICP-MS), except that ICP-MS has much lower detection limit (Karsson et al., 2015).

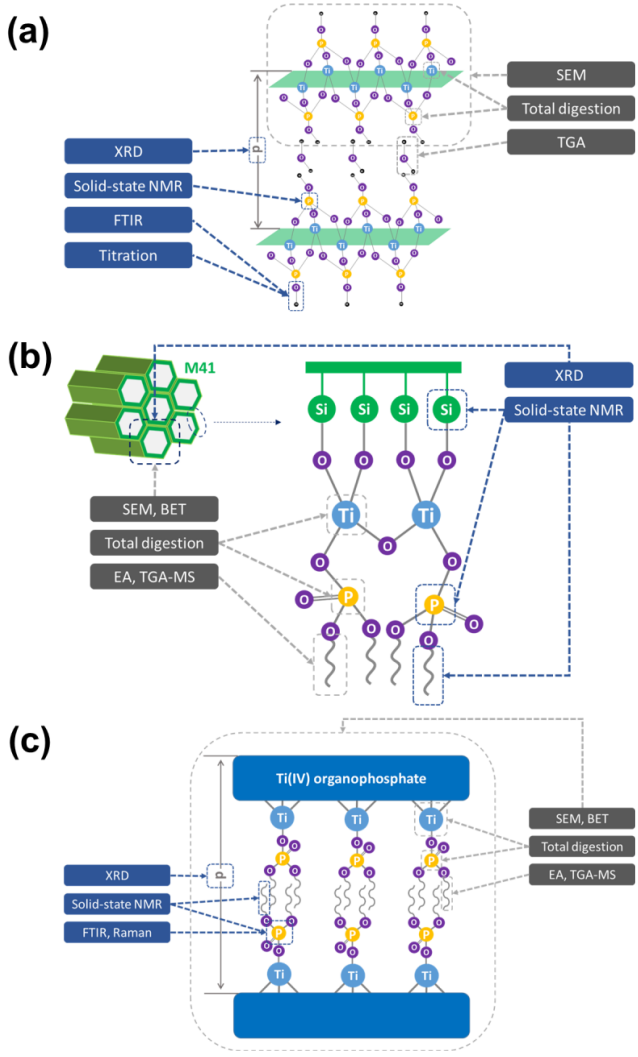
3.4.2 Column Experiments

The separation performance of the synthesised materials was further assessed on laboratory scale low-pressure chromatography columns (Bio-Rad). A peristatic pump equipped with silicone tubes were used for pumping the solution through the column. A Teledyne ISCO Retriever 500 fraction collector collected the effluent from the column before analysis. The glass columns were slurry-packed and pre-conditioned with acids to feed pH before operation. Detailed column operational conditions varied from one experiment to another and can be found in **articles I** and **II**.

4 Results and Discussion

4.1 Materials Characterisations

Understanding the morphological, compositional and structural characteristics is a necessity for the synthesised materials. These materials were characterised by bringing together different physicochemical and spectroscopic measurements. **Scheme 9** summaries the key characterisation methods used for each material.



Scheme 9.
Key characterisation methods linked to the local structure of the investigated materials. (a) Inorganic metal(IV) phosphates using α-TiP as an example. (b) M41 grafted titanium alkylphosphate materials. (c) Hybrid TiP materials. The curved lines attached to oxygen atoms represent alkyl chains.

4.1.1 Morphologies and Compositions

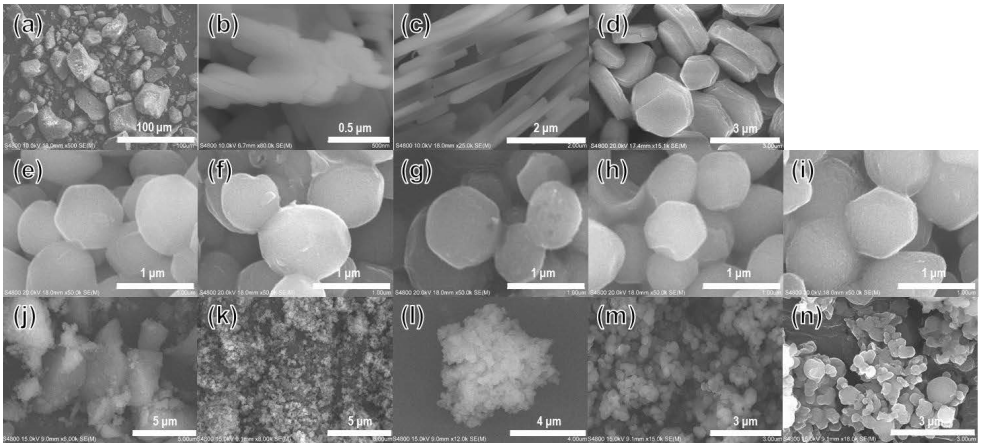


Figure 7. SEM images of the synthesised materials. (a) am-TiP. (b) α-TiP. (c) γ-TiP. (d) α-ZrP. (e) M41. (f) M41-TiP. (g) M41-TiEtP. (h) M41-TiPrP. (i) M41-TiBuP. (j) TiP_1:0. (k) TiP_3:1. (l) TiP_1:1. (m) TiP_1:3. (n) TiP_0:1.

Microscopic features are directly linked to the homogeneity, crystallinity and pore structure of the materials. Inorganic amorphous materials do not exhibit as regularly shaped particles (**Figure 7a**). Crystalline metal(IV) phosphates, however, were composed with highly ordered platelets (**Figure 7b–d**). The size and aspect ratio of the platelets are controllable through alternation in synthetic conditions (Sun et al., 2007). The phosphate concentration, synthesis route and presence of complexing agent affect the particle size of the final product. Refluxing in more concentrated phosphoric acid decreased the yield of the crystalline product while increased the particle size. Hydrothermal treatment in autoclaves (higher pressure) resulted in a significant growth of the particles compared to the refluxing method. The addition of F^- slowed down the hydrolysis of metal(IV), thus it favoured obtaining even larger particles. The synthesis conditions for metal(IV) phosphates in **articles I** and **II** are taken from literature with minor adaption. Theoretically, the particle sizes should only affect the kinetics of the ion-exchange reaction. In **article III**, the M41 silica (**Figure 7e**) and M41 grafted materials (**Figure 7f–i**) all featured hexagonal particles. They were formed through the condensation of silica under the presence of cationic surfactants and the structure was preserved after the layer-by-layer synthesis. The hybrid TiP materials studied in **article IV** are all practically

amorphous with interconnected spherical structure due to the self-assembly of the *n*-butyl chains (**Figure 7k–n**). Particle sizes first slightly decreased and then increased drastically with elevated organophosphate content. Note that the major difference in synthetic conditions between the TiP_1:0 (in **article IV, Figure 7j**) and am-TiP (in article **I, Figure 7a**) is that the former was synthesised in a water-ethanol mixture.

The contents of metal(IV) and phosphorus within the studied materials were assessed by total digestion followed with ICP-OES (**Table 6**). The crystalline materials have almost perfect phosphorus-to-metal(IV) ratios according to their formulae thus their compositions are not discussed here. The phosphorus-to-titanium(IV) ratio [*n*(P):*n*(Ti)] of am-TiP was determined to be close to one, meaning that it is rather a titanium hydroxylphosphate or oxohydroxylphosphate. The Ti and P contents as well as their ratios in M41 grafted titanium alkylphosphate materials were similar. A total of ca. 8% of Ti and ca. 4% of P was grafted onto the mesoporous support. The hybrid TiP series were synthesised from a precursor with a fixed *n*(P):*n*(Ti) ratio of two, however the final *n*(P):*n*(Ti) ratios increased with increased organophosphate content in the precursor.

Table 6. Titanium and phosphorus contents of the studied materials determined by total dissolution.

Material	Ti (wt.%)	P (wt.%)	Ti (mmol g^{-1})	P (mmol g^{-1})	*n*(P):*n*(Ti)
am-TiP	25.36	16.73	5.30	5.40	1.02
M41-TiP	8.38	4.04	1.75	1.30	0.74
M41-TiEtP	7.45	3.65	1.56	1.18	0.76
M41-TiPrP	8.09	3.86	1.69	1.24	0.73
M41-TiBuP	7.89	3.65	1.65	1.18	0.72
TiP_1:0	27.54	15.05	5.75	4.86	0.85
TiP_3:1	23.97	15.22	5.01	4.91	0.98
TiP_1:1	17.32	13.82	3.62	4.46	1.23
TiP_1:3	13.21	13.29	2.76	4.29	1.56
TiP_0:1	11.92	14.17	2.49	4.57	1.87

The composition of the materials was further studied with TGA, or TGA-MS when organic components were involved. The TiP materials underwent dehydration and dehydroxylation processes when heated in unreactive gas atmosphere. Free and crystal water were lost first, then the hydroxyl condensation happened.

Pyrophosphates were the final stable phase. TG was used to confirm the composition of crystalline TiPs in **article I**, and the results corresponded well with literature (Capitani et al., 2010; Andersen et al., 1998b). In **article III**, the evolved gas during TG treatment confirmed the successful grafting of *n*-alkyl chains. The cis elimination reaction of the alkylphosphate produced corresponding alkene which was directly measured by the flame ionisation mass detector. In the meantime, certain amounts of residual solvent and pyridine were detected. Same method was used for confirming the presence of butylphosphate groups in **article IV**, and this time no residual solvent was measurable. The cylindrical pore channels of the M41 grafted TiP materials contributed to the difficulty in a complete solvent removal. Detailed graphs and discussion of TG can be found in the articles.

4.1.2 Structure

The crystallinity of the materials was assessed by powder XRD (**Figure 8**). Crystalline TiPs and ZrP exhibited their typical patterns as indexed in the database. The synthesised γ-TiP was actually a mixture of γ-TiP and partially dehydrated γ'-TiP. The diameter of the pores in M41 materials is indicative by the diffraction peak of the (100) plane (**Figure 8b**). Layer-by-layer modification of the surface led to smaller pores. Grafting of longer alkyl chains did not necessarily lead to smaller pores since the coverage rates were not the same. The hybrid TiP materials are amorphous judged by the absence of high-intensity peaks (**Figure 8c**). The diffraction by self-assembled layers directed by the *n*-butyl chains in some of the hybrid materials was visible from XRD, and the peak position indicated the interlayer spacing of 1.41—1.51 nm.

The coordination environment of the phosphate groups within all the synthesised materials were studied by means of solid-state ^{31}P MAS NMR spectra recorded at room temperature (**Figure 9**). The spectra can be analysed by associating each ^{31}P resonance with a different phosphate connectivity (Schmutz et al., 1994). Protonation has only slight effect on the chemical shifts (±2 ppm). Typically, a ^{31}P resonance between -5 and -11 ppm is expected for $–H_2PO_4$ groups, while up to -25 ppm is observed for $–HPO_4$ groups owing to the geometrical and

local chemical differences of the ^{31}P sites (Trublet et al., 2016). Organic substitution has limited impact, thus the chemical shifts observed in HDBP and DBP are close to 0 ppm, which is the same as free H_3PO_4. For crystalline inorganic metal(IV) phosphate materials (**Figure 9a**), the ^{31}P NMR served as a purity check to ensure the absence of amorphous phase. This is an essential method for characterisation since small amounts of amorphous phase would not be detected by powder XRD. For amorphous TiP, the ratio of different phosphate groups could be estimated by peak deconvolution (**Figure 9a**). The situation was much more complicated with regards to the M41 grafted titanium alkylphosphate materials, where multiple overlapping peaks were present (**Figure 9b**). Peak assignments (**Table 7**) were therefore based on literature report (Kovalchuk et al., 2005). Approximately 40% of the P species were linked to surface Ti—O groups and 30-49% were modified onto Si—O groups. The different phosphate groups in the hybrid TiP materials were detected by ^{31}P NMR and quantified through peak deconvolution (**Figure 9c** and **Table 8**). The quantifications were made for inorganic phosphate only since the content of DBP could be more accurately measured by EA analysis, considering the carbon content.

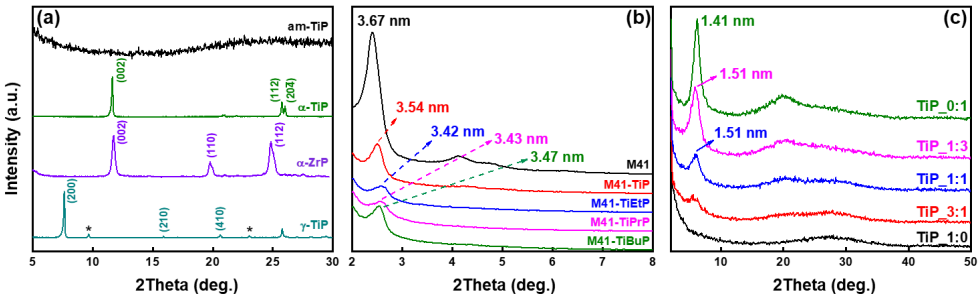


Figure 8. Powder XRD patterns of the synthesised materials in selected regions. (a) Inorganic metal(IV) phosphates with miller indices of the planes. (b) M41 grafted titanium alkylphosphate materials. (c) Hybrid TiP materials. The interplanar distances calculated by diffraction of (100) plane are marked in (b) and (c).

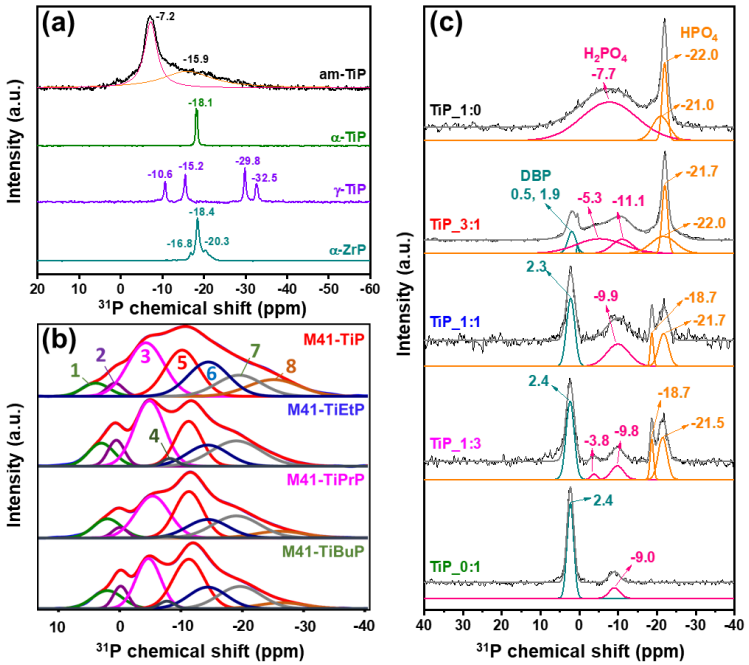


Figure 9. Solid-state ^{31}P MAS NMR spectra of the investigated materials. (a) Inorganic metal(IV) phosphates. (b) M41 grafted titanium alkylphosphate materials (peak assignments according to Table 7). (c) Hybrid TiP materials. Deconvolution peaks are shown where necessary.

Table 7. Assignments and relative quantification of P species in the M41 grafted TiP materials (R = H, Et, *n*-Pr or *n*-Bu).

Position *ca.* (ppm)	**Species**	**Relative quantification (%)**			
	(Peak number in Figure 9b)	M41-TiP	M41-TiEtP	M41-TiPrP	M41-TiBuP
0 and 2	≡SiO-**P**O(OR)2 **(1,2)**	8	16	13	15
-5 and -7.5	≡TiO-**P**O(OR)2 **(3,4)**	27	31	26	23
-11	(≡SiO)2-**P**O-(OR) **(5)**	21	18	23	27
-14.5	(≡TiO)2-**P**O-(OR) **(6)**	19	13	14	14
-19	Ti(H**P**O4)2 **(7)**	13	19	18	16
-26	Ti**P**2O7 **(8)**	12	3	6	5

Table 8. Assignments and relative quantification of P species in the hybrid TiP materials.

Materials	**HPO_4**		**H_2PO_4**		**DBP**
	ppm	%	ppm	%	ppm
TiP_1:0	-22.0, -21.0	27.6	-7.7	72.4	-
TiP_3:1	-22.0, -21.7	45.2	-5.3, -11.1	54.8	0.5, 1.9
TiP_1:1	-21.7, -18.7	46.4	-9.9	53.6	2.3
TiP_1:3	-21.5, -18.7	72.2	-3.8, -9.8	27.8	2.4
TiP_0:1	-	-	-9	100	2.3

Surface area measured by nitrogen porosimetry indicates the accessible porosity within the materials. The mesoporous M41 grafted titanium alkylphosphate materials featured high surface area (>300 $m^2 g^{-1}$), and the surface area decreased with functionalisation (**Table 9**). The pore width estimated by the BJH method was coherent with the interlayer spacing calculated by powder XRD. For the hybrid TiP materials, the surface area decreased with increased organophosphate content, and particles were growing accordingly. The pore width estimation here was not in the same order compared to powder XRD data, because nitrogen seemed not able to infiltrate into the hydrophobically assembled layers.

Table 9. Textural properties of the synthesised materials.

Material	d_{100}[a] (nm)	S_{BET}[b] ($m^2 g^{-1}$)	D_{pore}[c] (nm)	$D_{particle}$[d] (nm)
M41	3.67	1022	3.4	–
M41-TiP	3.54	879	3.4	–
M41-TiEtP	3.42	514	3.0	–
M41-TiPrP	3.43	443	3.0	–
M41-TiBuP	3.47	350	3.1	–
TiP_1:0	1.41	142	15.1	42.3
TiP_3:1	1.51	184	14.6	32.7
TiP_1:1	1.51	16.0	38.7	375.0
TiP_1:3	–	6.5	40.0	916.6
TiP_0:1	–	1.2	72.0	5168.2

[a]d_{100}: interplanar distance calculated by diffraction of (100) plane. [b]S_{BET}: BET specific surface area. [c]D_{pore}: average pore diameter estimated from the desorption branch by the BJH method. [d]$D_{particle}$: average particle size calculated by the DFT method.

Apart from the above-mentioned characterisations, FTIR (**articles I**, **III** and **IV**) and/or Raman spectroscopy (**article IV**) of certain materials were measured to gain information on the Ti—O or P—OH bonds. Titration by sodium hydroxide was conducted to determine the acidity and amount of the P—OH groups in the inorganic TiP materials (**article I**). Solid-state ^{1}H-^{13}C cross polarisation MAS NMR spectra confirmed the organic alkyl chains attached to the phosphate group (**articles III** and **IV**). Solid-state ^{29}Si MAS NMR spectra displayed the modification rate of surface silanol groups (**article III**). The calcined pyrophosphate phases were characterised by powder XRD (**articles I** and **IV**) and by Raman spectroscopy (**article IV**).

4.1.3 Summary

This section groups the same characterisation method for different materials together, aiming at illustrating the capability of each technique. For a specific material, the characterisation sections in the articles provide a more concise explanation.

In summary, the inorganic metal(IV) phosphate materials (**articles I** and **II**) were synthesised with well-established recipes and their crystallinities and purities were verified. Their formulae along with ion-exchange capacity and acid dissociation constants are listed in **Table 10**. Titanium alkylphosphate groups were successfully grafted onto the M41 support (article **III**), as confirmed by multiple characterisation methods. The mesoporosity of the materials were preserved. The hybrid TiP materials (article **IV**) were inorganic-organic amorphous coordination polymers assembled based on the hydrophobic interactions of the *n*-butyl chains. The formulae of the hybrid TiP materials were given in **Table 11**.

Table 10. Summary of chemical formulae and ion-exchange capacity for the inorganic metal(IV) phosphates.

Materials	**Formulae**	**Ion-exchange capacity (mequiv g^{-1})**		**pK_{a1}**	**pK_{a2}**
		Formula-calculated	NaOH titration		
am-TiP	$TiO_{1.11}(OH)_{0.58}(HPO_4)_{0.2}(H_2PO_4)_{0.8}\cdot 0.64H_2O$	9.79	5.6	-	-
α-TiP	$Ti(HPO_4)_2\cdot H_2O$	7.76	7.9	4.1	-
γ-TiP	$Ti(PO_4)(H_2PO_4)\cdot 0.96H_2O$	7.75	7.8	2.5	7.0
α-ZrP	$Zr(HPO_4)_2\cdot H_2O$	6.64	6.6*	3.3*	6.3*

* data obtained from Xu et al. (2017).

Table 11. Formulae and molecular weight for the hybrid TiP materials.

Materials	**Compound formulae**	**Molecular weight (g mol^{-1})**
TiP_1:0	$TiO_{0.02}(OH)_{2.88}(HPO_4)_{0.23}(H_2PO_4)_{0.62}\cdot 0.25H_2O$	183.9
TiP_3:1	$TiO_{0.43}(OH)_{1.84}(HPO_4)_{0.32}(H_2PO_4)_{0.39}(DBP)_{0.27}\cdot 0.24H_2O$	215.4
TiP_1:1	$TiO_{0.99}(OH)_{0.55}(HPO_4)_{0.24}(H_2PO_4)_{0.28}(DBP)_{0.71}\cdot 0.31H_2O$	277.4
TiP_1:3	$TiO_{1.05}(OH)_{0.13}(HPO_4)_{0.22}(H_2PO_4)_{0.07}(DBP)_{1.26}\cdot 0.10H_2O$	360.2
TiP_0:1	$TiO_{1.06}(OH)_{0.01}(H_2PO_4)_{0.24}(DBP)_{1.63}$	429.3

4.2 Batch Experiments

Batch separation experiments were conducted to test the research hypotheses and research ideas that directed the syntheses of the materials. The separation performance and mechanism were studied using simple batch systems coupled with further characterisations of the metal-loaded materials.

4.2.1 Titanium Phosphates

The core hypothesis to be tested in **article I** was size selection. The layered structure could serve as an ion-sieve for selective diffusion of the metal ions into the interlayer cavities. The metal cations essentially replace the H^+ within the P—OH groups of the inorganic TiP materials, resulting in the removal of the metal cations from the solution. As a result, the solution pH significantly affects the metal uptake since free H^+ competes with the process.

The most important separation task for the recovery of REEs from BR leachate is to separate Sc^{3+}, due to the high economic value of Sc. The effect of equilibrium pH on Sc^{3+} uptake was first studied on all three kinds of TiP materials (**Figure 10a**). Crystalline TiP materials showed increasing uptake with elevated pH, with the uptake on α-TiP surpassing that on γ-TiP. Considering the pK_a values in **Table 10**, γ-TiP should be more acidic and thermodynamically more favourable for Sc^{3+} ion exchange, compared to α-TiP. In addition, γ-TiP features larger basal spacing in between the layers, allowing easier diffusion of the Sc^{3+} ions. The experimentally observed uptake contradicted with the assumptions. It turned out that Sc^{3+} ions were not able to enter either the α- or γ-TiP layers, as the powder XRD patterns remained the same after Sc^{3+} uptake. Changes in metal forms of TiP should be clearly visible in XRD. The surface area therefore played a dominant role in determining the uptake amount. The α-TiP was made up by much smaller platelets compared with γ-TiP (**Figure 7b** and **7c**), therefore the former had larger surface area. For am-TiP, much higher Sc^{3+} uptake was observed (**Figure 10a**). The amorphous material allowed the utilisation of more surface ion-exchange sites. The uptake peak at pH 2 was attributed to the speciation of Sc^{3+}. The formation of

$Sc(OH)^{2+}$ starting from pH 2 and $Sc_2(OH)_2^{4+}$ from pH 3 explained the unusual pH—uptake curve (Baes and Mesmer, 1976).

The ion-exchange isotherms (**Figure 10b**) exhibited typical Langmuir type chemisorption shape with a clear plateau of the uptake. The total capacities for Sc^{3+}, as read from the isotherm, are 1.74, 0.55 and 0.22 mequiv g^{-1} for am-, α- and γ-TiP, respectively. The ratios of released H^+ to adsorbed Sc^{3+} were calculated for each isothermal point, and they were close to the stoichiometric value of three (**Figure 10c**). This indicated that the TiP materials were able to strip the hydroxyl layer away from Sc^{3+}.

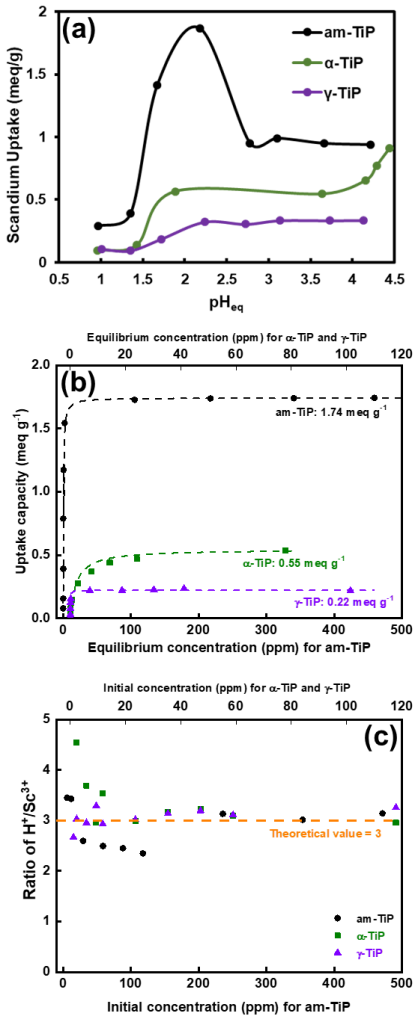


Figure 10. (a) Effects of solution equilibrium pH on Sc uptake of the TiP materials. (b) Sc^{3+} ion-exchange isotherms on the TiP materials at equilibrium pH 2.0 (±0.3). (c) The ratio of released H^+ to adsorbed Sc^{3+} as a function of initial Sc^{3+} concentration corresponding to the isotherms in (b).

Despite the unsuccessful utilisation of size selection, the metal ion selectivity was studied on the TiP materials. The excess amount of major metal ions in BR leachate, i.e. Al^{3+}, Fe^{3+}, Ti^{4+} and Na^{+} hinders the separation of Sc^{3+}. Among them, the most interfering ion for Sc^{3+} recovery is Fe^{3+} (Roosen et al., 2016). Tetravalent ions can be precipitated at low pH without sacrificing other components, and monovalent ions have lower affinity due to charge selection (Pan et al., 2007). A typical route for decreasing the affinity of Fe^{3+} on the ion-exchange materials is to reduce it to Fe^{2+}. Therefore, binary equimolar mixtures of Sc^{3+} and Al^{3+}, Ca^{2+}, Fe^{2+} or Y^{3+} were studied to understand the different ion-exchange behaviour of metal ions. The highest separation factors (**Figure 11**) were obtained from am-TiP at an equilibrium pH of 2, where the $SF_{Sc/Al}$ and $SF_{Sc/Y}$ were higher than 10^3 and the $SF_{Sc/Fe}$ was around 80.

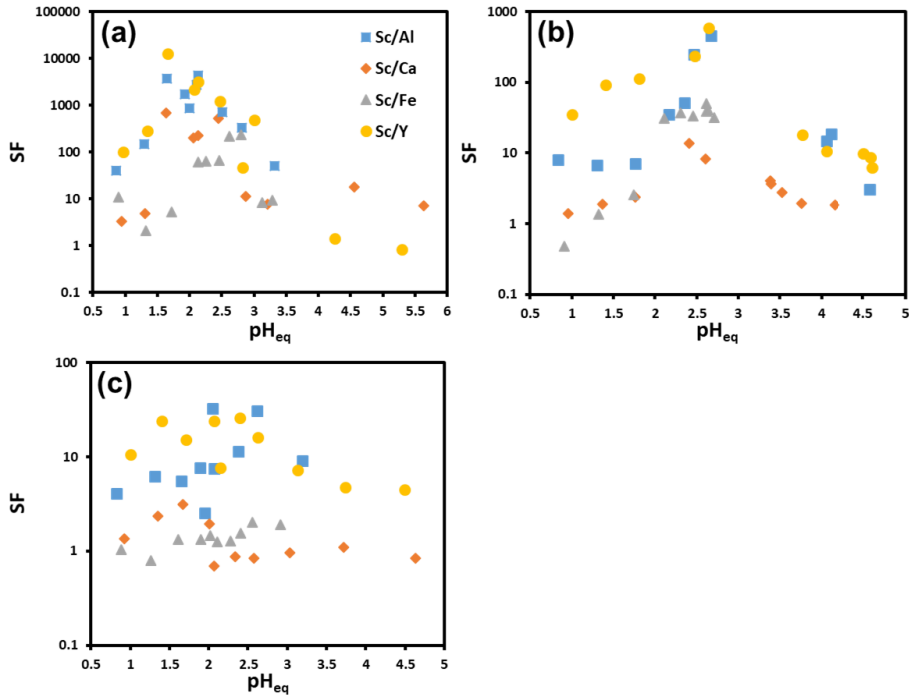


Figure 11. Separation factors obtained from 1 mM binary equimolar mixtures as a function of solution equilibrium pH on (a) am-TiP, (b) α-TiP and (c) γ-TiP.

The selectivity order (Fe^{2+} < Ca^{2+} < Al^{3+} < Sc^{3+}) of the metal ions on am-TiP did not follow their phosphate solubility order: *s*($FePO_4$) < *s*($AlPO_4$) < *s*($ScPO_4$) <

s[$Ca_3(PO_4)_2$] (Fernandez et al., 1999; Wood and Samson, 2006; Chang and Jackson, 1957). The 'solvation' of metal ions by P=O and P—OH groups is energetically more efficient compared to the coordination by water molecules (Strelko and Karaseva, 1977). The exchanged metal ions would be fully coordinated by the oxygen atoms to achieve minimum surface free energy. Ions that share a similar radius with the structural forming Ti should therefore be preferred by the ion-exchange process. The fact that the 6-coordinated ionic radius of Sc^{3+} (0.745 Å, according to Shannon, 1976) is the same as the 6-coordinated lattice radius of Ti^{4+} might explain the selectivity. This effect was more predominant in amorphous materials since the ion-exchange sites were more available to Sc^{3+}, due to the absence of long-range orders in the material lattice.

4.2.2 Zirconium Phosphate

Two research hypotheses were proposed in **article II**: (1) altered phosphate selectivity by using zirconium to replace titanium and (2) the formation of iron-chloro complexes to reduce Fe^{3+} loading. The target system was slightly different compared to article **I**. The focus of the work is to selectively recovery Sc^{3+} under the presence of Fe^{3+} at very low solution pH (<1.5) without reducing agents.

Firstly, am- and α- ZrP and TiP were tested with equimolar mixture of Fe^{3+} and Sc^{3+} to screen the selectivity under batch operation. Although the amorphous ion-exchangers exhibited higher uptake capacity (**Figure 12a and b**) for both Sc^{3+} and Fe^{3+} (especially am-ZrP), α-ZrP exhibited the highest $SF_{Sc/Fe}$ (**Figure 12c**). Increase in solution pH resulted elevated Fe^{3+} uptake and thus a decrease in the $SF_{Sc/Fe}$. As discussed in the earlier section, the acidity of the surface –OH groups is higher in TiP compared with ZrP, due to the higher polarising power of Ti^{4+}. It seemed that acidity was not the dominating factor in case of Sc^{3+} and Fe^{3+} ion exchange at low pH. According to Alberti et al. (1966), α-ZrP possesses higher free area around the phosphate group (24.0 $Å^2$) than α-TiP (21.6 $Å^2$) on the surface. The phosphate groups in ZrPs are more mobile owing to the lesser covalent nature of the Zr–O bonds compared to the Ti–O bonds. Higher free area and greater phosphate mobility are both convenient for accommodating larger species, and as the ionic

radius of Sc^{3+} is larger than that of Fe^{3+}, the uptake of Sc^{3+} was facilitated. Based on these observations, α-ZrP was selected for further studied.

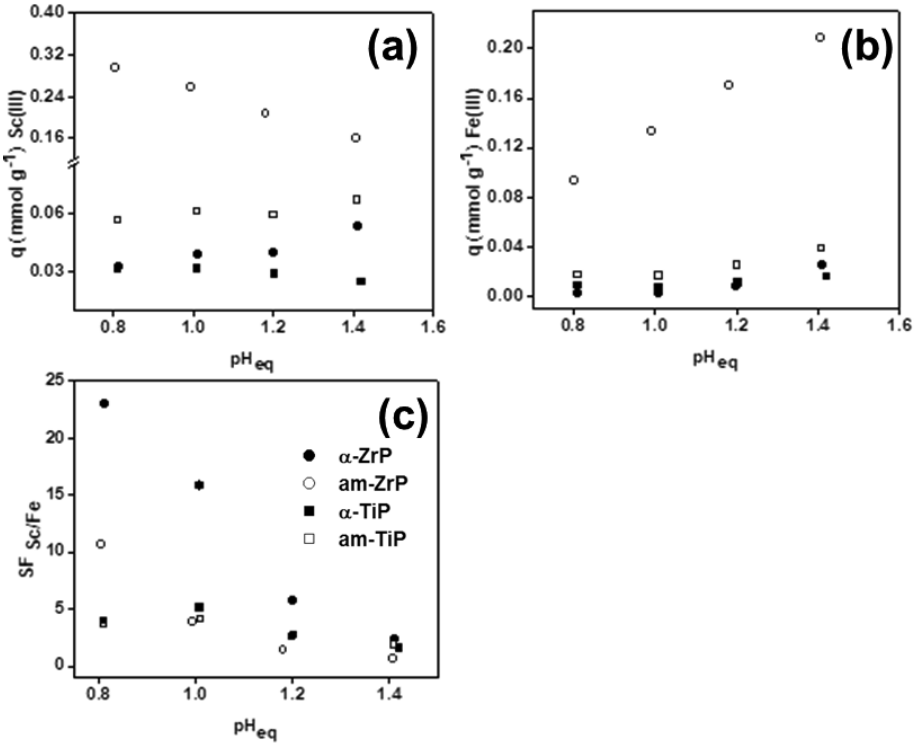


Figure 12. Sc^{3+} (a) and Fe^{3+} (b) uptake and separation factors (c) as a function of pH_{eq} with different inorganic ion-exchangers.

The second hypothesis (regarding the effect chloro complex) was tested by adding 3 M NaCl into the batch system. Alongside the formation of chloro complex which shifts the speciation of metal cations, also the effect of Na^+ has to be considered. By entering the layers of α-ZrP and possibly expanding the layer for subsequent trivalent ion-exchange, Na^+ acts as an ion-exchange reaction synergist. Indeed, the combined effect of Na^+ and Cl^- resulted in drastic increase of Sc^{3+} and Fe^{3+} uptake from single element solutions. The Sc^{3+} uptake increased from 0.10 mmol g^{-1} in unsalted solution to 0.60 mmol g^{-1} in 3 M NaCl at pH 1.0. Similar behaviour was observed for Fe^{3+}, thereby disproving the chloro complex hypothesis. The uptake increase should therefore result only from the effect of Na^+.

To further elucidate the uptake mechanism of Sc^{3+} and Fe^{3+} from HCl solutions with and without NaCl, additional studies on α-ZrP with Raman spectroscopy, extended X-ray absorption fine structure (EXAFS) and ^{31}P MAS NMR were attempted. Unfortunately, since the elemental content in the materials was not high enough, the spectra obtained by these techniques were inconclusive.

Practically, only in a narrow pH region, the calculated $SF_{Sc/Fe}$ from NaCl solutions significantly surpassed the separation factors obtained by the α-ZrP without NaCl addition (**Figure 13**). Therefore, the incremental selectivity enhancement of α-ZrP for Sc(III) with the addition of NaCl was not further explored. The salt addition would result in a more complex downstream process in practice. The α-ZrP was more selective for Sc^{3+} compared to Fe^{3+} in highly acidic solutions (pH < 1.5), which allowed for further column exploration with real BR leachate.

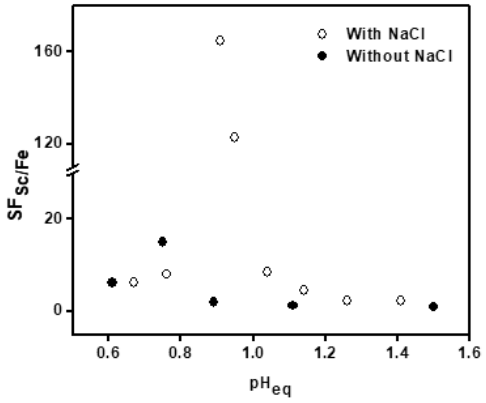


Figure 13. Sc/Fe separation factors with increasing pH_{eq} of Sc^{3+}-Fe^{3+} binary solutions with and without 3 M NaCl.

4.2.3 MCM-41 Silica Grafted Titanium Alkylphosphates

Since the ion-exchange sites inside the crystalline metal(IV) phosphate layers are unavailable to the REE ions, decorating the ion-exchange functional groups onto a mesoporous support material was tested in **article III**. The meso-scale pores of M41 (ca. 3 nm) are larger compared to the interlayer distance of the layered metal(IV) phsphates (ca. 1 nm). In addition, organophosphate groups were grafted onto the titanium modified M41 to mimic the structure of solvating extractants.

Whether the obtained materials behaved as solvating extractants is the

prerequisite phenomenon to be studied. Therefore, the binary batch systems composed by Sc^{3+} and La^{3+} were studied, with and without the addition of 5 M NH_4NO_3 as solvating agent. NH_4NO_3 was chosen as a proof-of-concept nitrate salt since it causes minimum matrix effect for metal analysis by ICP-OES or MP-OES. In industrial SX processes with TBP, $LiNO_3$ usually substitutes NH_4NO_3 because of the difficulties in treating ammonia-containing wastewater. The addition of salt clearly competed with the ion-exchange uptake of Sc^{3+} and La^{3+}, as lower K_d values were obtained in the salt-added systems for M41 and M41-TiP (**Figure 14a** and **14b**). The uptake of Sc^{3+} increased on the M41 grafted titanium alkylphosphate materials with 5 M NH_4NO_3 addition, and this confirmed the solvating extraction mechanism. The $SF_{Sc/La}$ of over 10^5 was obtained for M41-TiEtP and M41-TiPrP materials with salt addition (**Figure 14c**), demonstrating the excellent potential in separating them from each other. The immobilisation of solvating extraction ligands provided additional possibility for utilising extractants with shorter alkyl chains, since their high solubility in water hindered the use in typical SX systems.

Intralanthanide separation was tested on the M41 grafted titanium alkylphosphate materials by using an equimolar mixture of Nd^{3+} and Dy^{3+}. The solvating extraction behaviour was further demonstrated in **Figure 15a**, where there was practically no uptake for Nd^{3+} and Dy^{3+} by the inorganic materials (M41 and M41-TiP) under 5 M NH_4NO_3 condition. The uptake amount variations between materials with different length of alkyl chains were more likely due to the varied amounts of the grafted functional groups. The $SF_{Dy/Nd}$ was approximately three in all tested pH conditions (**Figure 15b, 15c** and **15d**), comparable to a solvent extraction system using TBP (Majdan, 1994). However, the capacity of such adsorbents is far lower than solvent extraction process, making them suitable for the recovery of REEs from dilute streams.

The selectivity of the solvating extraction could be explained by Lewis acid-base theory, in which REE ions are Lewis acids and form coordination bonds with phosphoryl groups (Lewis bases). The smaller the REE ion is, the stronger the Lewis acidity. Therefore, the selectivity sequence should and indeed appear as Sc^{3+} > Dy^{3+} > Nd^{3+} > La^{3+}. The formation of REE nitrate complex is not pH dependent

throughout our investigated pH range and the stability constants can be found in Andersson et al. (2006).

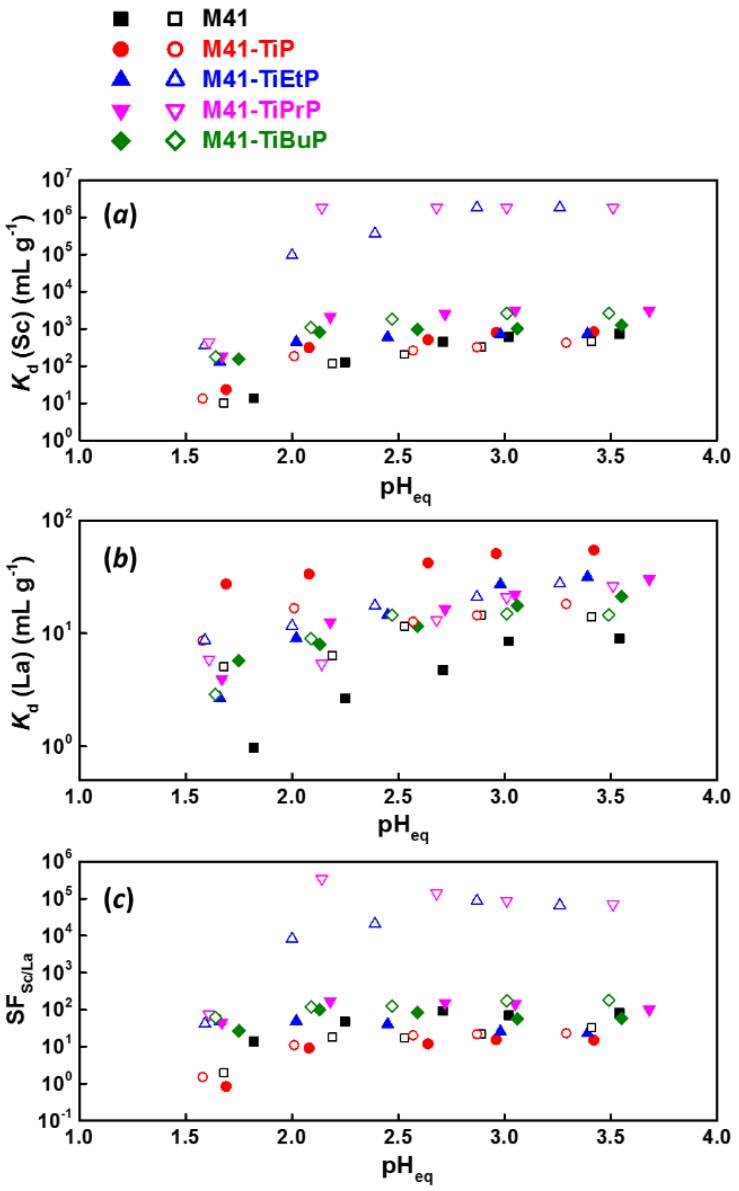


Figure 14. K_d values for Sc^{3+} (a) and La^{3+} (b) and the corresponding $SF_{Sc/La}$ values (c) as a function of equilibrium pH for sorption systems with 5 M NH_4NO_3 (open symbols) and without NH_4NO_3 (closed symbols).

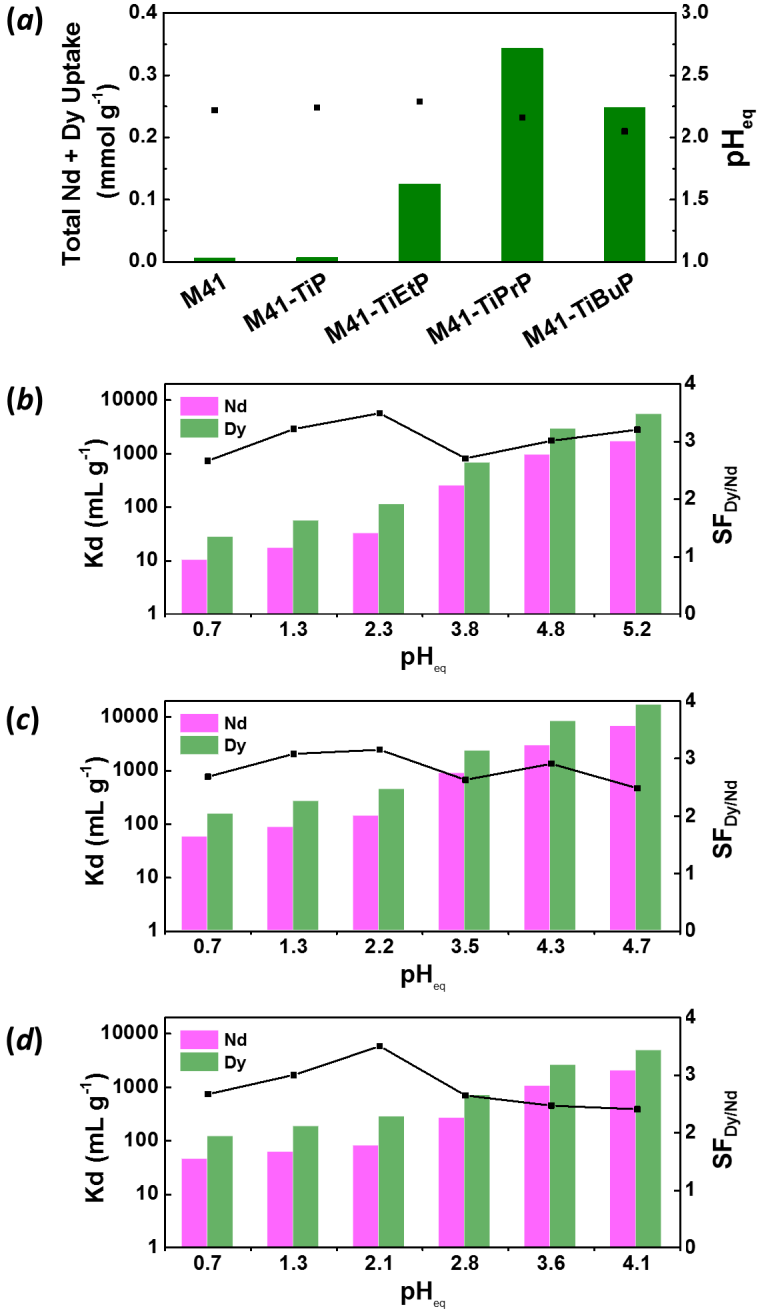


Figure 15. (a) Total Nd and Dy uptake under 5 M NH_4NO_3 (bars) and their corresponding equilibrium pH values (squares), K_d values (bars) and $SF_{Dy/Nd}$ (squares) as a function of equilibrium pH for (b) M41-TiEtP, (c) M41-TiPrP and (d) M41-TiBuP materials.

Hydrometallurgical operations require sufficient acid stability since the leachate is highly acidic. Pure siliceous materials are not suitable for such application due to their poor stability in strong acids. Titanium(IV) oxides and phosphates are less soluble in acid media (Shahadat et al., 2015) and therefore functionalising titanium(IV) derivatives to silica surface should increase the acid stability of the final material. The increased acid stability can be seen from **Table 12**.

Table 12. Acid stability of the pristine and the grafted M41 materials.[a]

Materials	0.1 M HNO_3 (pH 1)				0.01 M HNO_3 (pH 2)			
	Dissolved[b] Si		Dissolved Ti		Dissolved Si		Dissolved Ti	
	ppm	%	ppm	%[c]	ppm	%	ppm	%
M41	62.31	5.34%	-	-	21.9	1.88%	-	-
M41-TiP	6.15	0.53%	0.16	0.08%	3.71	0.32%	N.D.[d]	N.D.
M41-TiEtP	4.27	0.37%	0.08	0.04%	3.91	0.34%	N.D.	N.D.
M41-TiPrP	5.18	0.44%	0.12	0.06%	3.52	0.30%	N.D.	N.D.
M41-TiBuP	3.19	0.27%	0.09	0.05%	2.66	0.23%	N.D.	N.D.

[a] batch solid-to-liquid ratio: 50 mg / 20 mL acid, contact time: 6 h, [b] passed through 0.45 µm syringe filter, [c] percentage calculated based on elemental analysis results, [d] not detectable (<0.01 ppm).

4.2.4 Hybrid Titanium Butylphosphates

The organophosphate possessing M41 grafted materials showed solvating extraction capability, yet the organic grafting amount was not satisfactory. Therefore, in **article IV**, attempts were made by directly precipitating DBP with a titanium(IV) precursor, aiming at obtaining a solvating extraction material with higher loading capacity. The materials were synthesised through varying the organic-to-inorganic phosphate ratios in the synthesis liquor, and their structures were characterised.

Preliminary batch trials on competitive Nd-Dy uptake showed that higher materials with higher organophosphate contents separated better Nd^{3+} and Dy^{3+}. Hence, the selectivity towards the heavier Ln^{3+} by TiP_0:1 should originate from the organophosphate groups. Therefore, the lanthanide separation behaviour on TiP_0:1 material was further examined. The hybrid TiPs with higher inorganic phosphate content would find applications when total lanthanide uptake is needed.

The addition of 5 M NH_4NO_3 did not enhance the uptake of Nd^{3+} and Dy^{3+} on the TiP_0:1 material. The effect was rather uptake inhibition, thereby excluding the solvating extraction mechanism. To pinpoint the actual separation mechanism, the

Ti dissolution, pH changes and Ln^{3+} uptake were monitored in batch separation systems at different time intervals. For example, take a batch system composed with 2 mM Lu^{3+} at an initial pH of 1.8, the Ti dissolution (**Figure 16a**) and pH decrease (**Figure 16b**) could be clearly observed. The behavior suggested that Lu^{3+} uptake resulted from the transmetalation reaction: metal cation-exchange with intra-framework TiO^{2+}, according to **Scheme 10**. The ratio of dissolved Ti to Lu^{3+} uptake [n(Ti)/n(Lu^{3+})] in **Figure 16c** was always below the theoretical value at 1.5. The hydrolysis of Ti species led to decrease in the concentration of dissolved Ti, the solution pH, and the n(Ti)/n(Lu^{3+}) value.

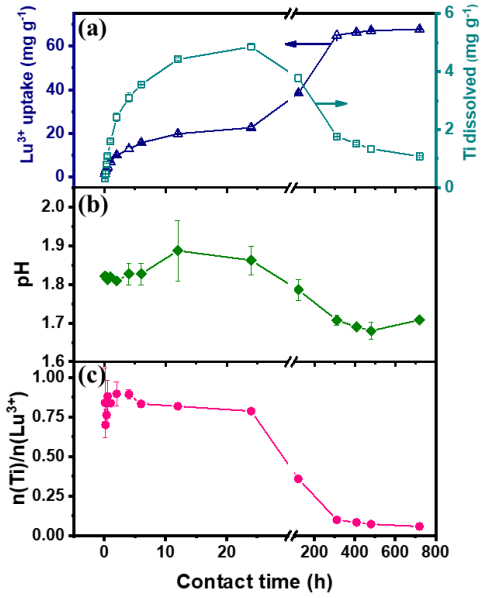
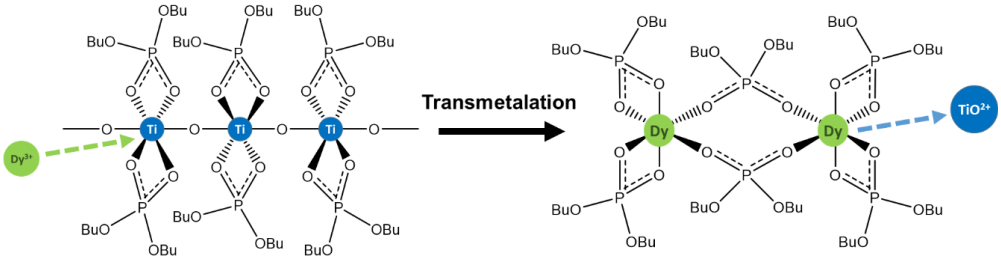


Figure 16. Lu^{3+} uptake kinetics on the TiP_0:1 material (2 mM Lu^{3+}). Effect of contact time on (a) Lu^{3+} uptake and Ti dissolution, (b) solution pH, and (c) n(Ti)/n(Lu^{3+}) ratio.



Scheme 10. Proposed transmetalation reaction on TiP_0:1 material demonstrating the exchange of framework TiO^{2+} with Dy^{3+}.

The transmetalation uptake preference of Ln^{3+} on the TiP_0:1 material was studied in a batch system composed with 10 mg L^{-1} of all REE^{3+} ions. The increase of equilibrium pH positively affected the uptake (**Figure 17**). The smallest ion, Sc^{3+}, was completely retained by the material already under pH 2.0. Across the Ln series, the extraction rate followed the "tetrad effect", with a clear dividing line between Gd and Tb. Our hypothesis for the extraction behaviour of Y^{3+} was that it should lie between those of Ho^{3+} and Er^{3+} since the ionic radii order for 6-coordinated ions appear as Ho^{3+} (90.1 pm) > Y^{3+} (90.0 pm) > Er^{3+} (89.0 pm). Indeed the hypothesis was proven in terms of extraction efficiency and K_d value.

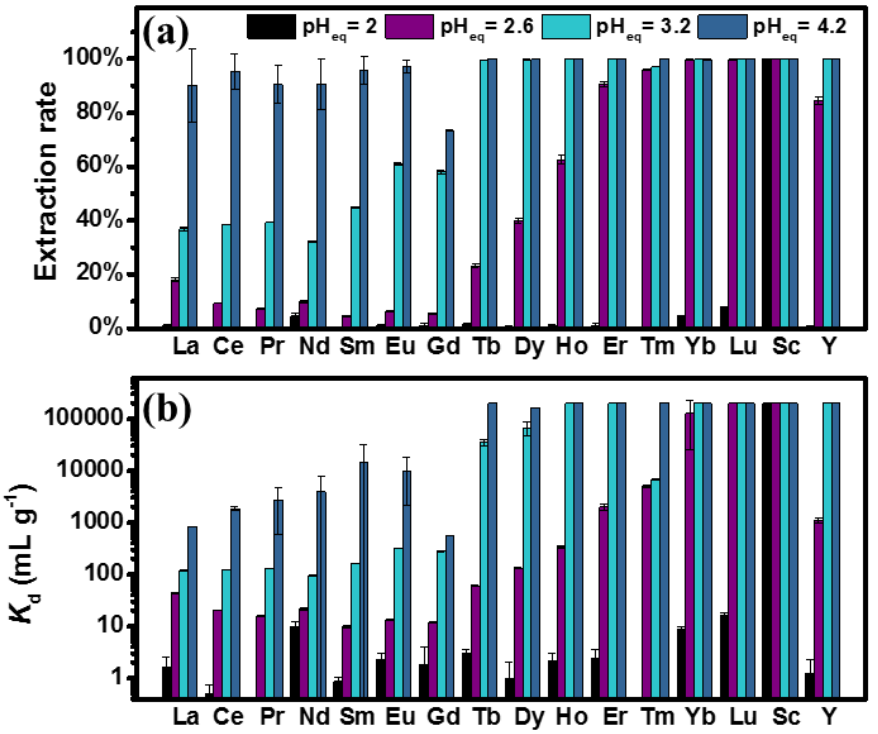


Figure 17. Extraction rates (a) and K_d values (b) for metal uptake on the TiP_0:1 material. The maximum K_d value in the study is presented as 199,800 mL g^{-1}, calculated from the detection limit (10 µg L^{-1}).

Binary Ln^{3+} uptake experiments were subsequently performed to assess the separation performance. Seven combinations were chosen: La-Ce, Pr-Nd, Eu-Gd, Gd-Tb, Tb-Dy, Yb-Lu, and Nd-Dy. Among these combinations, the first six

represented adjacent lanthanide pairs. Their separation performance was maximised by controlling the solution pH of the batch system, as the extraction of lanthanides exhibited pH-dependent behaviours. The lanthanide uptake affinity was explained by coordination preference and steric strain. Smaller lanthanide ions coordinate stronger with the DBP groups. The non-isostructural exchange of larger Ln^{3+} ions (86.1–103.2 pm, 6-coordinated) into the TiP framework (Ti^{4+} 74.5 pm) requires more energy due to the higher degree of structural distortion. Heavier and smaller Ln^{3+} in the pair was therefore always preferred to the solid phase. **Figure 18a** plots the optimal lanthanide molar fractions in the liquid and solid phases. After one batch cycle, the heavier lanthanide accounted for some 60–80% of the total lanthanide fraction in the solid phase. Concurrently, the lighter lanthanide was enriched in the liquid phase. The separation between Pr and Nd was the most difficult one in all studied pairs. This is no surprise since in SX processes, the extraction behaviours of Pr and Nd are extremely similar with a typical separation factor ($SF_{Nd/Pr}$) of 1.5 (He et al., 2018). Notably, nearly quantitative Nd-Dy separation was achieved batch-wise, as more than 99% of the loaded metal was Dy. The best achieved SF values (in logarithmic scale) was plotted against the difference in ionic radii for the binary batch separation systems in **Figure 18b**. It appeared that larger difference in the ionic radii positively influenced the separation performance.

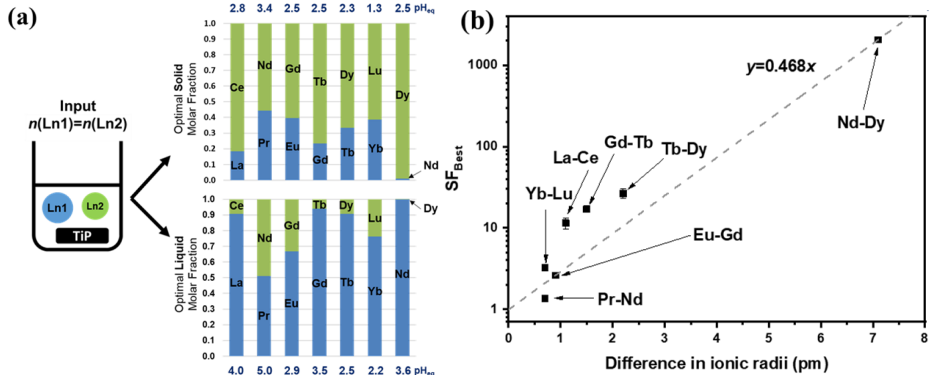


Figure 18. (a) Stacked column plots showing the optimal lanthanide fractions in the solid and the liquid phases obtained from the binary uptake study at different equilibrium pH values. (b) Dependence of the best achieved SFs with the ionic radii difference of the Ln^{3+} pairs.

4.3 Column Study

Laboratory scale column study employing simulated or real BR leachate was conducted to examine the separation performance under dynamic flow-through conditions. Usually, chromatographic separation results in better separation compared to the batch system since the loaded metal ion bands are allowed to undergo longer range of sorption-desorption cycles in the vertical column beds.

4.3.1 Amorphous Titanium Phosphate

A simulated BR leachate (**Table 13**) in pH 1.5 HNO_3 medium was prepared according to Roosen et al. (2016). By pre-conditioning the leachate pH to 2.0 with NaOH, all most all tetravalent ions (Si^{4+} and Ti^{4+}) were removed with minimum Sc^{3+} co-precipitation. By loading the leachate onto an am-TiP column, all other metal ions except Sc^{3+} and Fe^{3+} brokethrough the column after 4—5 BV. The interference of Fe^{3+} needed to be eliminated for better Sc^{3+} separation. Therefore, after loading the column with 8 BV of the pre-conditioned leachate, on-column reduction was performed. The column was rinsed with 2 BV of sodium sulphite solution (50 mM) to reduce the Fe^{3+} back to Fe^{2+}. Thereafter, acids were introduced onto the column for elution of the loaded metals (**Figure 19**). Most of the Fe and Al^{3+}, and all the Na^{+}, Ca^{+} and La^{3+} eluted with 0.2 M HNO_3. Increasing the HNO_3 concentration to 0.3 M further eluted some Fe and Al^{3+}, however ca. 10% of the loaded Sc^{3+} also started to come out of the column. Finally, eluting with a mixed acid (0.5 M equimolar mixture of HNO_3 and H_3PO_4) completely regenerated the column. Combining the final 30 BV of eluent (80—110 BV), the solution contained only Sc^{3+}, Fe^{3+} and Al^{3+} with concentrations of 0.35, 1.43 and 0.28 mg L^{-1}, respectively. Compared to the original leachate feed, the concentration ratio of Sc/Fe increased from 1/35 to 1/4, whereas the concentration ratio of Sc/Al increased from 1/318 to 1/1.2. Tandem column operations are expected to produce even purer Sc fractions, which will then be subject to oxalic acid precipitation to produce Sc oxide.

Table 13. Composition (mg L^{-1}) of the initial simulated HNO_3 BR leachate and the pre-conditioned leachate.

Leachate	Na	Ca	Al	Fe	Si	Ti	Sc	La
pH 1.5	1216	1069	641	94.3	572	95.7	2.01	5.30
pH 2.0	2232	1037	636	72.3	0.1	3.1	1.96	5.24

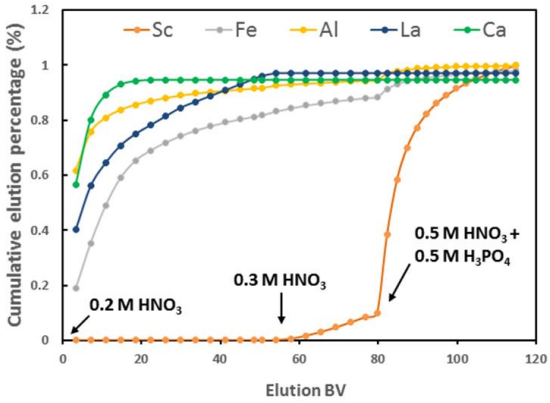


Figure 19. Elution chromatogram of simulated BR leachate-loaded am-TiP column using three different acid solutions.

4.3.2 α-Zirconium Phosphate

A total of 5 mL of freshly prepared BR leachate in HCl medium was loaded onto an α-ZrP column, filled with 1.0 g of the ion-exchanger. The composition of this leachate is highly challenging for subsequent separation, since only 1.9 mg L^{-1} of Sc^{3+} was present along with major metal ions in the concentrations that are several orders of magnitude higher (**Table 14**). During the loading process, most major metal ions were not loaded on the column. The α-ZrP column exhibited quantitative uptake for Sc^{3+}, while the second most retained metal is Fe^{3+}.

Table 14. Composition of the HCl BR leachate and recovery of elements by the α-ZrP column.

Elements	Concentration in the leachate (mg L^{-1})	Recovery (%)
Ca	5108	6.2
Al	2653	3.9
Si	1202	35.2
Fe	358	54.1
Ti	227	43.3
Ce	9.9	21.7
La	9.3	15.6
Nd	3.7	38.6
Sc	1.9	>99.9
Y	1.7	29.2
Dy	0.6	8.9

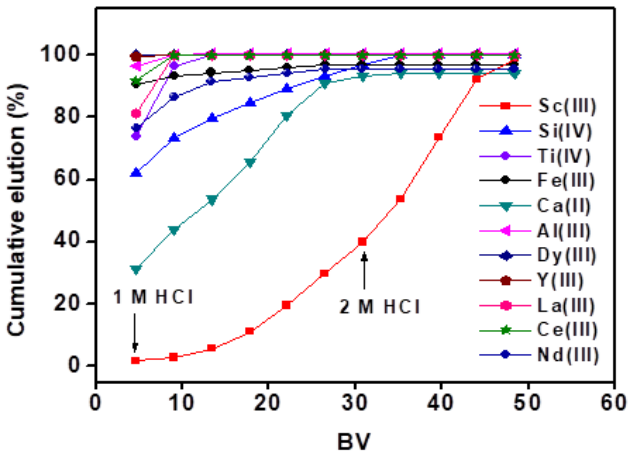


Figure 20. Cumulative elution of elements recovered by α-ZrP from BR HCl leachate. Feed: pH_{ini} = 2.2, V = 5 mL, flow rate 2 BV h^{-1}.

To separate Sc^{3+} from other co-loaded metals, a simple gradient elution with HCl was performed (**Figure 20**). Eluting the leachate-loaded α-ZrP column with 1 M HCl for 31 BV almost completely elute all the co-loaded metals, while 40% of the loaded Sc^{3+} was co-eluted. A stronger acid (2 M HCl) eluted the remaining 60% of Sc^{3+}, and in the last 17 BV of elution, no other impurities (including Fe^{3+}) were detected in this fraction. The column separation study served as a proof-of-concept work indicating that α-ZrP could offer a unique possibility for the direct recovery of Sc^{3+} from highly acidic BR leachates without any pre-treatment.

Both the column processes here are not optimised to fulfil the requirements of industrial applications, where there will be issues with large volumes of metal-containing acid wastewaters and how to recycle them efficiently inside the process.

5 Conclusions and Outlook

Metal(IV) phosphate-based materials were synthesised to target the REEs separation and recovery from aqueous acidic solution, with BR leachate as a focus.

Inorganic TiP materials bearing amorphous and layered crystalline structures exhibited suitable host structure for the separation of trace Sc^{3+} from complex BR acid leachate. The Sc^{3+} ions were not able to enter the interlayer cavities, therefore the separation performance of am-TiP (with larger accessible surface area) exceeded that of crystalline α- and γ-TiP. The selectivity towards Sc^{3+} was attributed to the matching between the lattice radius of Ti^{4+} and the ionic radius of Sc^{3+}. The column separation of Sc^{3+} from a simulated BR leachate was enhanced by on-column reduction of Fe^{3+} to Fe^{2+}. Through one cycle of chromatographic column operation, the ratios of Sc/Fe and Sc/Al were enriched by factors of 9 and 265, respectively, on an am-TiP column. Purer Sc^{3+} fraction could be expected by tandem column operations. Intercalation and pillaring of the TiP layers would potentially improve the accessibility of the ion-exchange moieties inside the layer, thereby increasing the overall capacity. However, care needs to be taken to maintain the acid-stability of the materials. It is interesting also to study the effect of platelet aspect ratio on the ion-exchange uptake of different metal ions to correlate the accessible surface area with the uptake.

Inorganic α-ZrP possessed good selectivity towards Sc^{3+} under the presence of high concentration of Fe^{3+}, without the need to reduce Fe^{3+}. Reasonably high separation factors for Sc/Fe were obtained at pH as low as 1.0. The addition of NaCl significantly enhanced the uptake of both Sc^{3+} and Fe^{3+}, which indicated the synergistic role of Na^{+} played in the overall ion-exchange process. The formation of chloro complexes did not result in evident decrease of the Fe^{3+} uptake. Trading the slightly increased separation factor with the addition of 3 M NaCl did not seem a reasonable option. Directly loading an α-ZrP column with a BR leachate resulted in a quantitative Sc^{3+} recovery, while most of the major metal ions were not retained. Using gradient elution by 1 and 2 M HCl solution, 60% of the Sc^{3+} was eluted as a final pure fraction. The powdery form of the material is not ideal for column

operation, as clogging and pressure drop can occur. Obtaining granular or composite form of the materials would provide more operational ease and higher throughput.

The feasibility of designing a hybrid composite material mimicking the structure of organophosphate solvent extractants was demonstrated through layer-by-layer surface grafting of the mesoporous M41 silica with titanium alkylphosphate functionalities. The M41 silica offered abundant surface reactive silanol groups for heteroatom functionalisation as well as improved contact efficiency in aqueous solution. The deposition of organophosphate groups via Ti—O—P bonds differed from traditional silylation route and provided enhanced acid resistance. The prepared M41 grafted titanium alkylphosphate materials indeed exhibited solvating extraction capability, to the extent that is comparable to TBP in SX systems. The batch separation between Sc^{3+} and Ln^{3+} was achievable on these hybrid materials. Further work on functionalisation of porous titania or zirconia can be envisioned. The use of longer and sterically hindered alkyl groups would probably result in fine-tuned selectivity towards specific REE ions.

Intralanthanide separation, especially the separation between early and late lanthanide elements, was attempted by transmetalation reaction on hybrid titanium organophosphate coordination polymers. This is an intra-framework ion-exchange reaction that sacrifices the central structural forming Ti(IV) to the solution. The selective lanthanide uptake was controlled by adjusting solution pH without any other energy input. The ligand coordination and steric strain preference during the transmetalation process explained the selectivity preference for smaller lanthanide ions. The transmetalation process was more selective compared to precipitation and solvent extraction utilising the same organophosphate ligand. By carefully selecting the central metal ions (size and valence) and organophosphorus ligand, a suite of new materials can be prepared with tuneable metal selectivity. The reversibility of the transmetalation reaction, i.e. the regeneration of the materials, needs to be studied and optimised. Employing phosphonate and phosphinate ligands would empower higher stability and more variety to the proposed separation route.

The work summarised here was initiated from inorganic metal(IV) phosphate materials, extended to surface grafted metal(IV) organophosphate materials, and ended in metal(IV) organophosphate coordination polymers. Each of the materials possessed metal ion uptake capability from aqueous solution, however the selectivity and uptake mechanism differed. The separation studies were linked to the recovery of REEs from BR leachate, a complex and challenging acidic medium. More work was focused on materials chemistry and solution chemistry, rather than hydrometallurgical separation process design and flowsheets. The materials prepared here could guide the future design and synthesis work for obtaining materials with task-specific selectivity and operational ease, which ultimately would be ripe for application in industrial scale processes.

References

Alberti, G., Torracca, E. and Conte, A. **1966**. Stoichiometry of Ion Exchange Materials Containing Zirconium and Phosphate. *Journal of Inorganic and Nuclear Chemistry*, 28 (2), 607—613.

Alberti, G., Cardini-Galli, P., Costantino, U. and Torracca, E. **1967**. Crystalline Insoluble Salts of Polybasic Metals—I Ion-Exchange Properties of Crystalline Titanium Phosphate. *Journal of Inorganic and Nuclear Chemistry,* 29, 571-578.

Alberti, G., Casciola, M., Costantino, U. and Vivani, R. **1996**. Layered and Pillared Metal(IV) Phosphates and Phosphonates. *Advanced Materials*, 8 (4), 291—303.

Alkan, G., Yagmurlu, B., Cakmakoglu, S., Hertel, T., Kaya, S., Gronen, L., Stopic, S. and Freidrich, B. **2018**. Novel Approach for Enhance Scandium and Titanium Leaching Efficiency from Bauxite Residue with Suppressed Silica Gel Formation. *Scientific Reports*, 8, 5676.

Andersen, A. M. K., Norby, P. and Vogt, T. **1998a**. Determination of Formation Regions of Titanium Phosphates; Determination of the Crystal Structure of β-Titanium Phosphate, $Ti(PO_4)(H_2PO_4)$, from Neutron Powder Data, *Journal of Solid State Chemistry*, 140, 266—271.

Andersen, A. M. K. and Norby, P. **1998b**. Structural Aspects of the Dehydration and Dehydroxylation of γ-Titanium Phosphate, γ-$Ti(PO_4)(H_2PO_4)\cdot 2H_2O$. *Inorganic Chemistry*, 37, 4313-4320.

Anderssen, S. Eberhardt, K., Ekberg, C., Liljenzin, J.-O., Nilsson, M. and Skarnemark, G. **2006**. Determination of Stability Constants of Lanthanide Nitrate Complex Formation Using a Solvent Extraction Technique. *Radiochimica Acta*, 94, 469—474.

Badwal, S. P. S., Ciacchi, F. T. and Milosevic, D. **2000**. Scandia-Zirconia Electrolytes for Intermediate Temperature Solid Oxide Fuel Cell Operation. *Solid State Ionics*, 136, 91—99.

Baes, C. F. and Mesmer, R. E. **1976**. Hydrolysis of Cations, Wiley.

Bandara, H. M. D., Field, K. D. and Emmert, M. H. **2016**. Rare Earth Recovery from End-of-Life Motors Employing Green Chemistry Design Principles. *Green Chemistry*, 18, 753—759.

Bao, C., Guo, Y., Song, L., Lu, H., Yuan, B. and Hu, Y. **2011**. Facile Synthesis of Poly(vinyl alcohol)/α-Titanium Phosphate Nanocomposite with Markedly Enhanced Properties. *Industrial & Engineering Chemical Research*, 50, 11109-11116.

Bhaumik, A. and Inagaki, S. **2001**. Mesoporous Titanium Phosphate Molecular Sieves with Ion-Exchange Capacity. *Journal of the American Chemical Society*, 123 (4), 691—696.

Binnemans, K., Jones, P. T., Blanpain, B., Van Gerven, T. and Pontikes, Y. **2015**. Towards Zero-Waste Valorisation of Rare-Earth Containing Industrial Process Residues: A Critical Review. *Journal of Cleaner Production*, 99, 17—38.

Binnemans, K., Jones, P. T., Muller, T. and Yurramendi, L. **2018**. Rare Earths and the Balance Problem: How to Deal with Changing Markets? *Journal of Sustainable Metallurgy*, 4 (1), 126—146.

Bogatyrev, B. A., Zhukov, V. V. and Tsekhovsky, Yu. G. **2009**. Formation Conditions and Regularities of the Distribution of Large and Superlarge Bauxite Deposits. *Lithology and Mineral Resources*, 44 (2), 135—151.

Borra, C. R., Pontikes, Y., Binnemans, K. and Van Gerven, T. **2015**. Leaching of Rare Earths from Bauxite Residue (Red Mud). *Minerals Engineering*, 76, 20—27.

Borra, C. R., Blanpain, B., Pontikes, Y., Binnemans, K. and Van Gerven, T. **2016**. Smelting of Bauxite Residue (Red Mud) in View of Iron and Selective Rare Earths Recovery. *Journal of Sustainable Metallurgy*, 2 (1), 28—37.

Cai, Q., Lin, W.-Y., Xiao, F.-S., Pang, W.-Q., Chen, X.-H. and Zou, B.-S. **1999**. The Preparation of Highly Ordered MCM-41 with Extremely Low Surfactant Concentration. *Microporous and Mesoporous Materials*, 32 (1–2), 1—15.

Capitani, D., Casciola, M., Donnadiio, A. and Vivani, R. **2010**. High Yield Precipitation of Crystalline α-Zirconium Phosphate from Oxalic Acid Solutions. *Inorganic Chemistry*, 49, 9409—9415.

Chang, S. and Jackson, M. **1957**. Solubility Product of Iron Phosphate. *Soil Science Society of America Journal*, 21, 265—269.

Chen, Zhanheng. **2011**. Global Rare Earth Resources and Scenarios of Future Rare Earth Industry. *Journal of Rare Earths*, 29 (1), 1—6.

Chowdhury, I. H. and Naskar, M. K. **2016**. Hexagonal Sheet-like Mesoporous Titanium Phosphate for Highly Efficient Removal of Lead Ions from Water. *RSC Advance*, 6, 67136—67142.

Clearfield, A. and Stynes, J. A. **1964**. The Preparation of Crystalline Zirconium Phosphate and Some Observations on Its Ion Exchange Behaviour. *Journal of Inorganic and Nuclear Chemistry, 26 (1), 117—129.*

Clearfield, A. and Smith, G. D. **1969**. The Crystallography and Structure of α-Zirconium Bis(monohydrogen orthophosphate) Monohydrate. *Inorganic Chemistry*, 8 (3), 431—436.

Clearfield, A. and Roberts, B. D. **1988**. Pillaring of Layered Zirconium and Titanium Phosphates. *Inorganic Chemistry*, 27, 3237—3240.

Das, D. P. and Parida, K. **2006**. Liquid Phase Bromination of Phenol Over Titania Pillared Zirconium Phosphate and Titanium Phosphate. *Catalysis Communications*, 7 (2), 68—72.

Digonnet, M. J. F. and Dekker, M. **2001**. *Rare-Earth-Doped Fiber Lasers and Amplifiers, Revised and Expanded*. CRC Press, Florida.

Ekambaram, S. and Sevov, S. C. **1999**. Organically Templated Mixed-Valent Ti^{III}/Ti^{IV} Phosphate with an Octahedral-Tetrahedral Open Framework. *Angewandte Chemie International Edition*, 38 (3), 372—375.

Espina, A., Garcia, J. R., Guil, J. M., Jaimez, E., Parra, J. B. and Rodriguez, J. **1998**. Calorimetric Study of Amine Adsorption on α- and γ-Titanium Phosphate. *Journal of Physical Chemistry*, 102, 1713—1716.

European Commission. **2017**. Study on the Review of the List of Critical Raw Materials: Criticality Assessments. Accessed May 2018 via https://publications.europa.eu/en/publication-detail/-/publication/08fdab5f-9766-11e7-b92d-01aa75ed71a1/language-en

Evans, K. **2016**. The History, Challenges, and New Developments in the Management and Use of Bauxite Residue. *Journal of Sustainable Metallurgy*, 2 (4), 316—331.

Fernandez, E., Gil, F., Ginebra, M., Driessen, F., Planell, J. and Best, S. **1999**. Calcium Phosphate Bone Cements for Clinical Applications. Part I: Solution Chemistry. *Journal of Materials Science: Materials in Medicine*, 10, 169—176.

Freeman, A. J. and Watson, R. E. **1962**. Theoretical Investigation of Some Magnetic and Spectroscopic Properties of Rare-Earth Ions. *Physical Review*, 127(6), 2058—2075.

Garcia-Glez, J., Trobajo, C., Khainakov, S. A. and Amghouz, Z. **2017**. α-Titanium Phosphate Intercalated with Propylamine: An Alternative Pathyway for Efficient Europium(III) Uptake into Layered Tetravalent Metal Phosphates. *Arabian Journal of Chemistry*, 10 (6), 885—894.

Gelencsér, A., Kováts, N., Turóczi, B., Rostási, Á., Hoffer, A., Imre, K., Nyirő-Kósa, I., Csákberényi-Malasics, D., Tóth, Á., Czitrovszky, A., Nagy, A., Nagy, S., Ács, A., Kovács, A., Ferincz, Á., Hartyáni, Z. and Pósfai, M. **2011**. The Red Mud Accident in Ajka (Hungary): Characterization and Potential Health Effects of Fugitive Dust. *Environmental Science & Technology*, 45 (4), 1608—1615.

He, Y., Chen, K., Srinivasakannan, C., Li, S., Yin, S., Peng, J., Guo, S. and Zhang, L. **2018**. Intensified Extraction and Separation Pr(III)/Nd(III) from Chloride Solution in Presence of a Complexing Agent Using a Serpentine Microreactor. *Chemical Engineering Journal*, 354, 1068—1074.

Hind, A. R., Bhargava, S. K. and Grocott, S. C. **1999**. The Surface Chemistry of Bayer Process: A Review. *Colloids and Surfaces A: Physicochemical and Engineering Aspects*, 146 (1-3), 359—374.

Henderson, P. **1984**. *Rare Earth Element Geochemistry* (Vol. 2), Elsevier.

International Aluminium Institute **2015**. Bauxite Residue Management: Best Practice. *Accessed on 9th July 2018 via http://www.world-aluminium.org/media/filer_public/2015/10/15/bauxite_residue_management_-_best_practice_english_oct15edit.pdf*

International Aluminium Institute **2018**. Statistics of Alumina Production. *Accessed on 10th July 2018 via http://www.world-aluminium.org/statistics/alumina-production/*

IUPAC. **2005**. Nomenclature of Inorganic Chemistry: IUPAC Recommendations 2005. RSC Publishing.

Jiao, X., Chen, D., Pang, W., Xu, R. and Yue, Y. **1998**. Solvothermal Synthesis and Characterization of Silica-Pillared Titanium Phosphate. *Journal of Materials Chemistry*, 8, 2931—2834.

Johansson, N., Krook, J., Eklund, M. and Berglund, B. **2013**. An Integrated Review of Concepts and Initiatives for Mining the Technosphere: Towards a New Taxonomy. *Journal of Cleaner Production*, 55, 35—44.

Jones, D. J., Aptel, G., Brandhorst, M., Jacquin, M., Jimenez-Jimenez, J., Jimenez-Lopez, A., Maireles-Torres, P., Piwonski, I., Rodriguez-Castellon, E., Zajac, J. and Roziere, J. **2000**. High Surface Area Mesoporous Titanium Phosphate: Synthesis and Surface Acidity Determination. *Journal of Materials Chemistry*, 10, 1957—1963.

Jorjani, E. and Shahbazi, M. **2016**. The Production of Rare Earth Elements Group via Tributyl Phosphate Extraction and Precipitation Stripping Using Oxalic Acid. *Arabian Journal of Chemistry*, 9 (2), S1532—S1539.

Karlsson, S., Sjöberg, V. and Ogar, A. **2015.** Comparison of MP-AES and ICP-MS for Analysis of Principal and Selected Trace Elements in Nitric Acid Digests of Sunflowre (*Helianthus annuus*). *Talanta*, 135, 124—132.

Kovalchuk, T., Sfihi, H., Korchev, A., Kovalenko, A., Ilin, V., Zaitsev, V. and Fraissard, J. **2005**. Synthesis, Structure, and Acidic Properties of MCM-41 Functionalized with Phosphate and Titanium Phosphate Groups. The Journal of Physical Chemistry B, 109 (29), 13948—13956.

Kumar, S., Kumar, R. and Bandopadhyay, A. **2006**. Innovative Methodologies for the Utilisation of Wastes from Metallurgical and Allied Industries. *Resources, Conservation and Recycling*, 48 (4), 301—314.

Kul, M., Topkaya, Y. and Karakaya, I. **2008**. Rare Earth Double Sulfates from Pre-Concentrated Bastnasite. *Hydrometallurgy*, 93, 129—135.

Llavona, R., Suarez, M., Garcia, J. R. and Rodriguez, J. **1989**. Lamellar Inorganic Ion Exchangers. Alkali Metal Ion Exchange on α- and γ- Titanium Phosphate. *Inorganic Chemistry*, 29, 2863—2868.

Li, C., Huang, Y. and Lin, Z. **2014**. Fabrication of Titanium Phosphate@Graphene Oxide Nanocomposites and Its Super Performance on Eu^{3+} Recycling. *Journal of Materials Chemistry A*, 2, 14979—14985.

Li, X. S., Courtney, A. R., Yantasee, W., Mattigod, S. V. and Fryxell, G. E. **2006**. Templated Synthesis of Mesoporous Titanium Phosphates for the Sequestration of Radionuclides. *Inorganic Chemistry Communications*, 9 (3), 293—295.

Liu, Y., Naidu, R. **2014**. Hidden Values in Bauxite Residue (Red Mud): Recovery of Metals. *Waste Management*, 34, 2662—2673.

Lucy, C. A. **2003**. Evolution of Ion-Exchange: From Moses to the Manhattan Project to Modern Times. *Journal of Chromatography A*, 1000 (1–2), 711—724.

Majdan, M. **1994**. The Separation Factors of the Lanthanides in the $Ln(NO_3)_3$-NH_4NO_3-TBP System. Effects of Change in Activity Coefficients. *Hydrometallurgy*, 35, 179—185.

Marin Rivera, R., Ulenaers, B., Ounoughene, G., Binnemans, K. and Van Gerven, T. **2018**. Extraction of Rare Earths From Bauxite Residue (Red Mud) by Dry Digestion Followed by Water Leaching, *Minerals Engineering*, 119, 82—92.

McLennan, S. M. **1994**. Rare Earth Element Geochemistry and the "Tetrad" Effect. *Geochimica et Cosmochimica Acta*, 58 (9), 2025—2033.

Pan, B., Zhang, Q., Du, W., Zhang, W., Pan, B., Zhang, Q., Xu, Z. and Zhang, Q. **2007**. Selective Heavy Metal Removal from Waters by Amorphous Zirconium Phosphate: Behavior and Mechanism. *Water Research*, 41, 3103—3111.

Pasechnik, L. A., Tyutyunnik, A. P., Enyashin, A. N., Baklanova, I. V., Yatsenko, S. P., Dyachkova, T. V., Medyankina, I. S. and Skachkov, V. M. **2017**. Synthesis and Crystal Structure of 3*R* and 1*T*' Polytypes of $NH_4Sc(SO_4)_2$, *Journal of Solid State Chemistry*, 255, 50—60.

Pasechnik, L. A., Tyutyunnik, A. P., Enyashin, Samigulina, R. F., Ilyina, E. A., Skachkov, V. M., Medyankina, I. S. and Yatsenko, S. P. **2018**. Polymorphism and Properties of Ammonium Scandium Sulfate $(NH_4)_3Sc(SO_4)_3$: New Intermediate Compound in Scandium Production. *CrystEngComm*, 20, 3772—3783.

Pica, M. **2017**. Zirconium Phosphate Catalysts in the XXI Century: State of the Art from 2010 to Date. *Catalysts*, 7 (6), 190.

Pica, M., Donnadio, A. and Casciola, M. **2018**. From Microcrystalline to Nanosized α-Zirconium Phosphate: Synthetic approaches and Applications of An Old Material with A Bright Future. *Coordination Chemistry Reviews*, 374 (1), 218—235.

Pietrelli, L. Bellomo, B., Fontana, D. and Montereali, M. R. **2002**. Rare Earths Recovery From NiMH Spent Batteries. *Hydrometallurgy*, 66 (1—3), 135—139.

Pontikes, Y. and Angelopoulos, G. N. **2013**. Bauxite Residue in Cement and Cementitious Applications: Current Status and a Possible Way Forward. *Resources, Conservation and Recycling*, 73, 53—63.

Porvali, A., Wilson, B. P. and Lundström, M. **2018**. Lanthanide-Alkali Double Sulfate Precipitation From Strong Sulfuric Acid NiMH Battery Waste Leachate. *Waste Management*, 71, 381—389.

Power, G., Gräfe, M. and Klauber, C. **2011**. Bauxite Residue Issues: I. Current Management, Disposal and Storage Practices. *Hydrometallurgy*, 108, 33—45.

Peppard, D. F., Manson, G. W. and Lewey. S. **1969**. A Tetrad Effect in the Liquid-Liquid Extraction Ordering of Lanthanides(III). *Journal of Inorganic and Nuclear Chemistry*, 31 (7), 2271—2272.

Queneau, P. B. and Berthold, C. E. **1986**. Silica in Hydrometallurgy: an Overview. *Canadian Metallurgical Quarterly*, 25 (3), 201—209.

Ren, T.-Z., Yuan, Z.-Y., Azioune, A., Pireaux, J.-J. and Su, B.-L. **2006**. Tailoring the Porous Hierarchy of Titanium Phosphates. *Langmuir*, 22 (8), 3886—3894.

Ricketts, N. J. and Duyvesteyn W. P. **2018**. Scandium Recovery from the Nyngam Laterite Project in NSW. In *TMS Annual Meeting & Exhibition*. Springer, Cham, pp 1539—1543.

Rivera, V. A. G., Ferri, F. A. and Marega Jr, E. **2012**. Localized Surface Plasmon Resonances: Noble Metal Nanoparticle Interaction with Rare-Earth Ions. In *Plasmonics-Principles and Applications*. InTech, pp 294.

Roosen, J., Van Roosendael, S., Borra, C., Van Gerven, T., Mullens, S. and Binnemans, K. **2016**. Recovery of Scandium from Leachates of Greek Bauxite Residue by Adsorption on Functionalized Chitosan–Silica Hybrid Materials. *Green Chemistry*, 18, 2005—2013.

Roskill. **2016**. *Rare Earths: Global Industry, Markets and Outlook* (16th ed.). Roskill, London, United Kingdom.

Schmutz, C., Barboux, P., Ribot, F., Taulelle, F., Verdaguer, M. and Fernandez-Lorenzo, C. **1994**. EXAFS, Raman and ^{31}P NMR Study of Amorphous Titanium Phosphates. *Journal of Non-Crystalline Solids*, 170, 250—262.

Shahadat, M., Teng,T. T., Rafatullah, M. and Arshad, M. **2015**. Titanium-Based Nanocomposite Materials: A Review of Recent Advances and Perspectives. *Colloids and Surfaces B: Biointerfaces*, 126, 121—137.

Shannon, R. D. **1976**. Revised Effective Ionic Radii and Systematic Studies of Interatomic Distances in Halides and Chalcogenides. *Acta Crystallographica Section A*, 32, 751—767.

Silbernagel, R., Martin, C. H. and Clearfield, A. **2016**. Zirconium(IV) Phosphonate–Phosphates as Efficient Ion-Exchange Materials. *Inorganic Chemistry*, 55 (4), 1651—1656.

Strelko, V. and Karaseva, T. **1977**. On Causes of Specific Sorption of Ions on Inorganic Ion Exchangers of Zirconium Phosphate Type. *Adsorbtsiya I Adsorbenty*, 5, 71—77.

Suarez, M., Garcia, J. R. and Rodriguez, J. **1984a**. Thermodynamic Treatment of H^+/Na^+ Ion Exchange on α-Titanium Phosphate. *Journal of Physical Chemistry*, 88, 159—162.

Suarez, M., Garcia, J. R. and Rodriguez, J. **1984b**. Calorimetric Determination of H^+/Na^+ Ion Exchange on α-Titanium Phosphate. *Journal of Physical Chemistry*, 88, 157—159.

Sun, L., Boo, W. J., Browning, R. L., Sue, H.-J. and Clearfield, A. **2005**. Effect of Crystallinity on the Intercalation of Monoamine in α-Zirconium Phosphate Layer Structure. *Chemistry of Materials*, 17, 5606—5609.

Sun, L., Boo, W. J., Sue, H.-J. and Clearfield, A. **2007**. Preparation of α-Zirconium Phosphate Nanoplatelets with Wide Variations in Aspect Ratios. *New Journal of Chemistry,* 31, 39—43.

Sun, L., O'Reilly, J. Y., Kong, D., Su, J. Y., Boo, W. J., Sue. H.-J. and Clearfield. A. **2009**. The Effect of Guest Molecular Architecture and Host Crystallinity upon the Mechanism of the Intercalation Reaction. *Journal of Colloid and Interface Science*, 333 (2), 503—509.

Taylor, S. R. and McClennan, S. M. **1981**. The Composition and Evolution of the Continental Crust: Rare Earth Element Evidence from Sedimentary rocks. *Philosophical Transactions of the Royal Society A*, 301 (1461), 381—399.

Taylor, S. R. and McClennan, S. M. **1985**. The Continental Crust: Its Composition and Evolution. Blackwell Scientific Publications, Oxford, United Kingdom.

Thieme, M. and Schuth, F. **1999**. Preparation of a Mesoporous High Surface Area Titanium Oxo Phosphate via a Non-Ionic Surfactant Route. *Microporous and Mesoporous Materials*, 27 (2-3), 993—200.

Tompkins, E. R., Khym, J. X. and Cohn, W. E. **1947**. Ion-Exchange as a Separations Method. I. The Separation of Fission-Produced Radioisotopes, Including Individual Rare Earths, by Complexing Elution from Amberlite Resin. *Journal of the American Chemical Society*, 69 (11), 2769—2777.

Trublet, M., Maslova, M. V., Rusanova, D. and Antzutkin, O. N. **2016**. Mild Syntheses and Surface Characterization of Amorphous $TiO(OH)(H_2PO_4)\cdot H_2O$ Ion-Exchanger. *Materials Chemistry and Physics*, 183, 467—475.

Trublet, M., Rusanova, D. and Antzutkin, O. N. **2018**. Revisiting Syntheses of $Ti(IV)/H_2PO_4$–HPO_4 Functional Ion-Exchangers, Properties and Features. *New Journal of Chemistry*, 42, 838—845.

Tunsu, C., Petranikova, M., Gergoric, M., Ekberg, C. and Retegan, T. **2015**. Reclaiming Rare Earth Elements from End-of-Life Products: A Review of the Perspectives for Urban Mining Using Hydrometallurgical Unit Operations. *Hydrometallurgy*, 156, 239—258.

U. S. Geological Survey. **2018**. *Mineral Commodity Summaries*. Accessed May 2018 via https://minerals.usgs.gov/minerals/pubs/mcs/2018/mcs2018.pdf

Vind, J., Malfliet, A., Blanpain, B., Tsakiridis, P. E., Tkaczyk, A. H., Vassiliadou, V. and Panias, D. **2018a**. Rare Earth Element Phases in Bauxite Residue. *Minerals*, 8 (77), 1—32.

Vind, J., Malfliet, A., Bonomi, C., Paiste, P., Sajo, I. E., Blanpain, Tkaczyk, A. H., Vassiliadou, V. and Panias, D. **2018b**. Modes of Occurrences of Scandium in Greek Bauxite and Bauxite Residue. *Minerals Engineering*, 123, 35—48.

Wang, W. and Cheng C. Y. **2011**. Separation and Purification of Scandium by Solvent Extraction and Related Technologies: a Review. *Journal of Chemical Technology and Biotechnology*, 86, 1237—1246.

Wang, X., Yang, X., Cai, J., Miao, T., Li, L., Li, G., Deng, D., Jiang, L. and Wang, C. **2014**. Novel Flower-Like Titanium Phosphate Microstructures and Their Application in Lead Ion Removal from Drinking Water. *Journal of Materials Chemistry A*, 2, 6718—6722.

Wang. X., Zhao, D., Medina, I. B. N., Diaz, A., Wang, H., Clearfield, A., Mannan M. S. and Cheng, Z. **2016**. Surface Modification of Layered Zirconium Phosphate with PNIPAM. *Chemical Communications*, 52, 4832—4835.

Wood, S. A. and Samson, I. M. **2006**. The Aqueous Geochemistry of Gallium, Germanium, Indium and Scandium. *Ore Geology Reviews*, 28, 57—102.

Xie, F., Zhang, T. A., Dreisinger, D. and Doyle, F. **2014**. A Critical Review on Solvent Extraction of Rare Earths from Aqueous Solutions. *Minerals Engineering*, 56, 10—28.

Xu, J., Wiikinkoski, E., Koivula, R., Zhang, W., Ebin, B. and Harjula, R. **2017**. HF-Free Synthesis of α-Zirconium Phosphate and Its Use as Ion Exchanger for Separation of Nd(III) and Dy(III) from a Ternary Co–Nd–Dy System. *Journal of Sustainable Metallurgy*, 3 (3), 646—658.

Xu, J., Koivula, R., Zhang, W., Wiikinkoski, E., Hietala, S. and Harjula, R. **2018**. Separation of Cobalt, Neodymium and Dysprosium Using Amorphous Zirconium Phosphate. *Hydrometallurgy*, 175, 170—178.

Yagmurlu, B., Dittrich, C. and Friedrich, B. **2017**. Precipitation Trends of Scandium in Synthetic Red Mud Solutions with Different Precipitation Agents. *Journal of Sustainable Metallurgy*, 3 (1), 90—98.

Yagmurlu, B., Dittrich, C. and Friedrich, B. **2018**. Effect of Aqueous Media on the Recovery of Scandium by Selective Precipitation. *Metals*, 8, 314.

Zepf., V. **2013**. Rare Earth Elements: What and Where They Are. In *Rare Earth Elements*. Springer, Berlin, Heidelberg, pp 11—39.

Zhang, J., Ma, Z., Jiao, J., Yin, H., Yan, W., Hagaman, E. W., Yu, J. and Dai, S. **2009**. Layer-by-Layer Grafting of Titanium Phosphate onto Mesoporous Silica SBA-15 Surfaces: Synthesis, Characterization, and Applications. *Langmuir*, 25 (21), 12541—12549.

Zhou, Y., Huang, R., Ding, F., Brittain, A. D., Liu, J., Zhang, M., Min, X., Meng, Y. and Sun, L. **2014**. Sulfonic Acid-Functionalized α-Zirconium Phosphate Single-Layer Nanosheets as a Strong Solid Acid for Heterogeneous Catalysis Applications. *ACS Applied Materials & Interfaces*, 6 (10), 7417—7425.

Zhou, Y., Wang, A., Wang, Z., Chen, M., Wang, W., Sun, L. and Liu, X. **2015**. Titanium Functionalized α-Zirconium Phosphate Single Layer Nanosheets for Photocatalyst Applications. *RSC Advances*, 5, 93969—93978.

Zhu, Y., Yoneda, K., Kanamori, K., Takeda, K., Kiyomura, T., Kurata, H. and Nakanishi, K. **2016**. Hierarchically Porous Titanium Phosphate Monoliths and Their Crystallization Behavior in Ethylene Glycol. *New Journal of Chemistry*, 40, 4153—4159.